RESEARCH ARTICLE

Key Points:
- The centrifugal force accelerates particles during outward flux tube expansion
- Nonadiabatic flux tube expansion occurs at Jupiter between noon and dusk LT
- These effects can explain why Jupiter's plasma sheet thickens from 12 to 18 LT

Correspondence to:
M. F. Vogt,
marissav@ucla.edu

Simulating the effect of centrifugal forces in Jupiter's magnetosphere

Marissa F. Vogt[1,2], Margaret G. Kivelson[3,4,5], Krishan K. Khurana[3,4], Raymond J. Walker[3,4,6], Maha Ashour-Abdalla[3,7], and Emma J. Bunce[1]

[1]Department of Physics and Astronomy, University of Leicester, Leicester, UK, [2]Formerly at Department of Earth and Space Sciences and Institute of Geophysics and Planetary Physics, University of California, Los Angeles, California, USA, [3]Institute of Geophysics and Planetary Physics, University of California, Los Angeles, California, USA, [4]Department of Earth, Planetary, and Space Sciences, University of California, Los Angeles, California, USA, [5]Department of Atmospheric, Oceanic, and Space Science, University of Michigan, Ann Arbor, Michigan, USA, [6]National Science Foundation, Arlington, Virginia, USA, [7]Department of Physics and Astronomy, University of California, Los Angeles, California, USA

Abstract Jupiter's large scale size and rapid planetary rotation period combine to produce the strong centrifugal force responsible for many unique properties of its magnetosphere. It was previously proposed that this centrifugal force and nonadiabatic field line stretching could cause the observed dawn-dusk asymmetry of Jupiter's plasma sheet, which is thickest near dusk. As flux tubes rotate and stretch between noon and dusk, particles bouncing along the field gain parallel energy and create pressure anisotropy. Because bounce times can be long compared with the outward expansion timescale, particles may respond nonadiabatically, and the resulting pressure anisotropy can drive the plasma sheet to instability. We used a large-scale kinetic simulation to follow a collection of rotating particles as they move in a time-varying, rotating magnetic field designed to represent flux tube expansion in Jupiter's magnetosphere. The analysis quantifies the response of trapped particles by characterizing the pressure anisotropy and energy changes. We compare results of nonadiabatic and adiabatic outward expansions and find that the nonadiabatic case leads to a large pitch angle anisotropy and higher total energy than for adiabatic expansion. Although the calculation was not handled fully self-consistently, the results support the proposition that plasma pressure changes lead to changes in the magnetic field structure with local time. Our findings are consistent with the idea that nonadiabatic effects in Jupiter's magnetosphere contribute to field dipolarization and the observed plasma sheet thickening between noon and dusk.

1. Introduction

In the Earth's magnetosphere, gravitational and centrifugal forces are small compared to magnetic forces and can usually be ignored when considering particle motion. However, in Jupiter's magnetosphere, centrifugal forces are important owing to the combination of three factors: large scale sizes (the average magnetopause standoff distance is ~75 Jovian radii or R_J, where 1 $R_J = 71,492$ km), a fast planetary rotation period (~10 h), and the fact that much of the plasma consists of heavy ions (oxygen and sulfur) as opposed to protons. As a result, the corotational energy per particle, $\frac{m\rho^2\Omega^2}{2}$, where m is the particle mass, ρ is cylindrical radial distance, and Ω is the rotation frequency, for ions in the middle magnetosphere can be comparable to or larger than the thermal energy. For example, the corotational energy of a 20 m_p (proton mass) particle at $\rho = 40$ R_J is ~26 keV, while the thermal energy estimates range from ~1–2 keV to ~80 keV [*Frank and Paterson*, 2002, 2004; *Kane et al.*, 1995].

Centrifugal forces influence many features of Jupiter's magnetosphere. For example, in the inner magnetosphere the plasma density along a flux tube decreases exponentially with distance from the centrifugal equator, the point on each field line farthest from the spin axis, due to confinement by the centrifugal force [*Hill and Michel*, 1976; *Bagenal et al.*, 1980; *Bagenal and Sullivan*, 1981]. Centrifugal stresses are also thought to be the dominant factor driving tail dynamics and plasmoid release at Jupiter [*Vasyliūnas*, 1983]. Finally, *Kivelson and Southwood* [2005] have proposed that the centrifugal force energizes particles during the nonadiabatic field line stretching which occurs as flux tubes rotate between noon and dusk, resulting in the observed dawn-dusk asymmetry of the plasma sheet thickness.
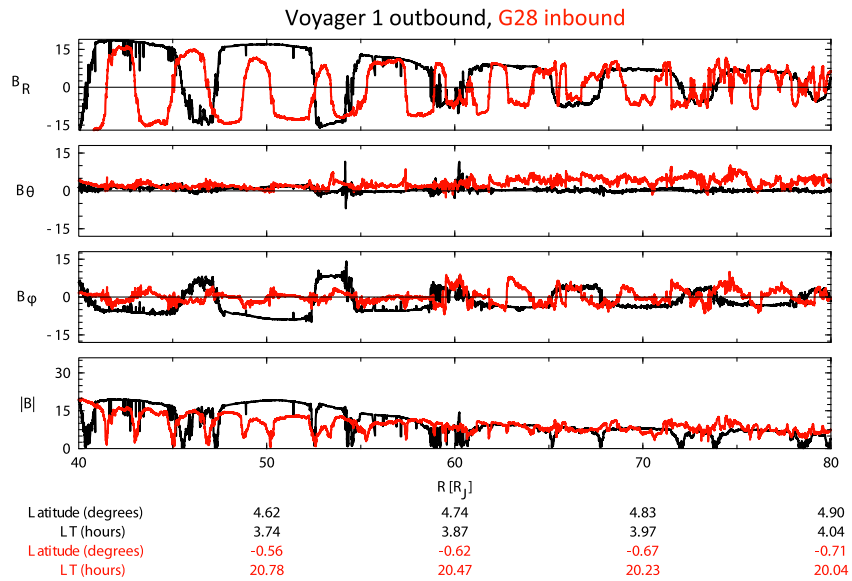
Figure 1. Magnetic field data in System III coordinates from Voyager 1 outbound (black lines), in the dawn local time sector, and Galileo orbit G28 inbound (red lines), near dusk, plotted versus radial distance in Jovian radii. The magnetic field is in units of nanoTesla. The plasma sheet is much thicker for G28 than for Voyager 1, as evidenced by the larger B_θ and more disordered radial field.

We have developed a large-scale kinetic (LSK) simulation that quantifies some of the key physical processes invoked by *Kivelson and Southwood* [2005]. An LSK simulation assumes properties of the electromagnetic field and tracks the temporal evolution of test particles having different initial energies, pitch angles, and starting points using the Lorentz force law. In the simulation we follow a collection of rotating particles on a representative flux tube in the middle magnetosphere in a time-varying magnetic field in which the equatorial crossing points of flux tubes move steadily outward. This reproduces the outward displacement that occurs in the magnetosphere as flux tubes rotate from noon to dusk. The simulation provides a proof of principle for the physical processes that occur in Jupiter's magnetosphere. The results illustrate how the energy and pitch angle distributions may change in response to the centrifugal force and nonadiabatic field line stretching.

2. Plasma Sheet Thickness: Observations and Proposed Explanations

2.1. Local Time Asymmetries in Jupiter's Plasma Sheet

The plasma in Jupiter's middle and outer magnetosphere is concentrated in a hinged plasma sheet. Between 10 and 30 R_J the plasma sheet is aligned with the magnetic equator [*Behannon et al.*, 1981], which is tilted 9.6° with respect to the jovigraphic equator. From 30 to 60 R_J, the plasma sheet is located between the centrifugal and magnetic equators, whereas beyond ~60 R_J it runs parallel to the solar wind [*Khurana*, 1992]. Jupiter's plasma sheet exhibits strong local time asymmetries, being thickest near dusk and thinnest in the postmidnight to dawn local time sector [*Kivelson and Khurana*, 2002; *Waldrop et al.*, 2005]. The typical half thickness is ~2–3 R_J near dawn and more than 6 R_J near dusk [*Khurana*, 1992; *Khurana and Schwarzl*, 2005]. High-latitude observations from Ulysses near dusk suggest a very thick plasma sheet that would account for periodic plasma sheet signatures encountered more than ~25 R_J off of the jovigraphic equator [*Lanzerotti et al.*, 1993].

Figure 1 presents magnetic field data from Voyager 1 near dawn (black lines) and Galileo orbit G28 inbound near dusk (red lines) as a function of radial distance, illustrating the dawn-dusk differences in the plasma sheet thickness and magnetic field configuration. The envelope of the field magnitude as a function of distance is roughly the same at both local times, except for a transient increase near ~50–55 R_J in the Voyager 1 data. However, the meridional component of the magnetic field, B_θ, is larger near dusk than near dawn by a factor of 2 or more (even near the center of the plasma sheet), especially beyond ~55 R_J. Assuming vertical stress balance, the plasma sheet thickness is proportional to the vertical component of the magnetic field (similar to B_θ), so that a stronger $|B_\theta|$ suggests a thicker plasma sheet near dusk than near dawn

[e.g., *Khurana and Kivelson*, 1989]. The envelope of the radial component of the magnetic field, B_R, is roughly equal for both local times, but $|B_\theta/B_R|$ is larger at dusk, indicating a more dipolar and less stretched field configuration, suggestive of a thicker plasma sheet, at dusk than at dawn. Both spacecraft remained near the jovigraphic equator (magnetic latitude $\pm \sim 10°$). Voyager 1 encountered the relatively thin dawnside plasma sheet about every 5 h, as evidenced by the periodic minima in the field magnitude and regular reversals in B_R. By comparison, for orbit G28, Galileo remained in or near regions of high plasma density, as evidenced by the relatively disordered duskside radial field.

2.2. Why Does the Plasma Sheet Thicken in the Postnoon Sector?

Some of the local time changes in the plasma sheet thickness can be understood in terms of proximity to the magnetopause. We expect the plasma sheet to be thinnest on the nightside, where field lines are unconstrained by the magnetopause and are highly stretched, in part due to centrifugal forces. Between the dawn flank and noon, the magnetopause distance decreases by roughly one fourth (~ 85 to $\sim 63\ R_J$ for the compressed case or ~ 127 to $\sim 92\ R_J$ for the expanded case) [*Joy et al.*, 2002]. The observed plasma sheet thickening that occurs between dawn and noon can then be explained as a response to increased normal pressure of the solar wind as local time increases and the magnetopause distance decreases. However, this argument does not explain the observed dawn/dusk asymmetry, as the same argument would lead one to expect that the plasma sheet would thin from noon to dusk in response to the reduced normal pressure of the solar wind with increase of local time and distance to the magnetopause.

One proposal attributes the dawn/dusk asymmetry in the plasma sheet thickness to the asymmetric distribution of open flux across the magnetotail, as would be observed if convection in Jupiter's magnetotail were restricted to a single cell on the dawn side [*Cowley et al.*, 2003; *Khurana et al.*, 2004]. This single-cell convection may be expected because corotation would oppose sunward return flow from tail reconnection in the dusk sector but would act to enhance the return flow in the dawn sector. As a result, the azimuthal flow would be expected to be slowest at dusk and faster at dawn, as is observed in flow velocities derived from Galileo's energetic particle detector (EPD) measurements [*Krupp et al.*, 2001]. A larger B_θ near dusk than near dawn would arise naturally because flux transport must be equal across the dawn and dusk meridians in the steady state, and flux transport is proportional to $\int v_\varphi B_\theta r dr$, where r is radial distance and v_φ is the azimuthal velocity. However, one cannot tell whether B_θ becomes large because the flow has slowed as outlined above or whether the flow slows because B_θ is large for some reason other than the change of flow speed, such as a thickening of the plasma sheet.

A different explanation for the dawn/dusk asymmetry comes from *Kivelson and Southwood* [2005]. They suggest that the duskside plasma sheet heating and associated thickening is a kinetic effect resulting from the combined effects of centrifugal forces imposed by Jupiter's rapid rotation and the nonadiabatic field line stretching that occurs as the magnetopause distance increases between noon and dusk. Their argument stems from the fact that a bouncing, rotating particle will gain parallel energy from the centrifugal force as it moves outward to a larger radial distance. As flux tubes rotate from noon to dusk, particles on an expanding field line move to larger values of ρ and the centrifugal force could produce a net increase in parallel energy. A key point is that over a relevant range of energies, particle bounce times in the middle magnetosphere are long compared with the time scale for field line expansion, which can further enhance the increase in the average parallel energy (see section 3.2). Because the centrifugal force increases only the parallel energy, it can create a pressure anisotropy which leads to what *Kivelson and Southwood* [2005] call a "centrifugal instability" in the plasma sheet.

The force density imposed on the plasma in the direction perpendicular to the magnetic field is given by

$$\mathbf{F}_\perp = -\nabla_\perp \left[p_\perp + \frac{B^2}{2\mu_0} \right] + \left(p_\parallel - p_\perp - \frac{B^2}{\mu_0} \right) \frac{\mathbf{R}_C}{R_C^2} + \rho_m \left(\Omega^2 \mathbf{r} - 2\mathbf{\Omega} \times \mathbf{v} \right)_\perp , \qquad (1)$$

where B is the magnetic field strength, $p_\perp, p_\parallel$ are the pressure tensor components (with respect to the magnetic field), μ_0 is the permeability of free space, $\mathbf{R}_C$ is the vector radius of curvature of the field line, ρ_m is mass density, $\mathbf{r}$ is the particle's radial distance from the center of Jupiter, and $\mathbf{v}$ is velocity in the rotating frame. Near the center of the outer plasma sheet, R_C at the equator is small compared to the radial distance r; for example, in the field model described in section 4.3, $R_C \approx 3.5\ R_J$ for the field line that crosses the equator at $r = 40\ R_J$. As Kivelson and Southwood note, the first term in equation (1) is of order $O(p_\perp/r)$, while the second term is of order $O(p_\perp/R_C)$, so the second term dominates near the center of the plasma sheet, and force balance requires $p_\parallel - p_\perp - \frac{B^2}{\mu_0} \approx 0$. When the parallel pressure increases enough that $p_\parallel > p_\perp + \frac{B^2}{\mu_0}$, the firehose

instability develops, leading to chaotic magnetic structure in the outer plasma sheet on the afternoon side. For example, in Figure 1, the reversals in the sign of B_R evident in the Voyager data acquired near 04:00 LT are highly regular at all distances from 40 to 80 R_J. However, in the Galileo data acquired near 20:00 LT, the B_R reversals are highly organized only inside of ~60 R_J and become extremely irregular, as if the sheet has started to flap at random times, beyond ~70 R_J. This suggests that the firehose instability has developed in the outer magnetosphere as *Kivelson and Southwood* [2005] speculated. The distortion of the field is capable of transferring parallel to perpendicular pressure and reducing the equatorial curvature of the average field configuration, thus thickening the plasma sheet (Figure 2).

2.3. Motivating Questions for This Work

In order to test the *Kivelson and Southwood* [2005] interpretation of plasma sheet thickening, our simulation must quantify how energy and pitch angle distributions on a rotating flux tube change in response to nonadiabatic flux tube expansion. As discussed in section 3.1, whether the total energy of the plasma increases or decreases due to field line stretching in a rotating system depends on many factors, including the initial particle distributions in energy, space, and pitch angle; the magnetic field geometry; and the temporal and spatial scales of the field line expansion. In order to investigate the response that is likely to develop in Jupiter's middle magnetosphere, we developed a kinetic simulation in which we track the motion of bouncing, rotating particles on an expanding flux tube to establish how the system responds. The simulation addresses the following questions:

1. How do centrifugal forces and field line stretching in Jupiter's magnetosphere affect the plasma energy distribution and pitch angle distribution?
2. If there is a net gain in energy or increase in pressure anisotropy ($p_\parallel > p_\perp$), is it sufficient to explain the observed plasma sheet thickening from noon to dusk?
3. What are the consequences of nonadiabatic behavior because the time scale for field line stretching can be short compared with particle bounce periods?
4. How are the results influenced by the initial plasma energy, pitch angle, and spatial distribution?

The analysis does not satisfy self-consistency of field and particle properties, a feature that should be incorporated in a future study. Furthermore, the simulation does not test the alternate theory that sunward return flow from tail reconnection at a distant neutral line opposes the dusk corotational flow, causing B_θ to increase and the duskside plasma sheet to thicken.

3. Effect of Flux Tube Expansion in a Rotating System

In order to understand the energy and pitch angle evolution of our simulated collection of particles, we must first establish how particle energy in a rotating system changes under outward radial expansion. Appendix A first reviews how the centrifugal force affects particle energy and bounce motion on a magnetic field that is static in the rotating frame. Throughout this study we assume rigid rotation but do not assume full corotation. For this section only we also follow *Northrop and Birmingham* [1982] and assume, unless explicitly stated, that $\mathbf{E} \cdot \mathbf{B} = 0$, where $\mathbf{E}$ is the electric field, and that the magnetic field $\mathbf{B}$ has no time dependence other than rigid rotation, so that $\nabla \times \mathbf{E} = 0$. In section 4 we work with magnetic field models that are not constant in time, so that the adiabatic invariants are not necessarily conserved.

3.1. Particle Energy Changes Under Adiabatic Flux Tube Expansion

Adiabatic flux tube expansion, in which a field line's equatorial crossing point moves radially outward, can be described in terms of an appropriately defined azimuthal electric field, which provides an $\mathbf{E} \times \mathbf{B}$ drift that carries the plasma on the flux tube radially outward. In the case of a time stationary magnetic field, the electric field is derivable from a scalar potential ϕ such that

$$\mathbf{E} = -\nabla\phi. \tag{2}$$

Conservation of the adiabatic invariants μ and J requires that the outward drift occur slowly compared to particle bounce and gyroperiods [*Northrop and Teller*, 1960]. Appendix B describes the effects of adiabatic expansion for particles on a nonrotating flux tube in the inertial frame. In general, adiabatic expansion results in lower energy, as a particle's perpendicular energy decreases to conserve μ and the parallel energy decreases to conserve J.
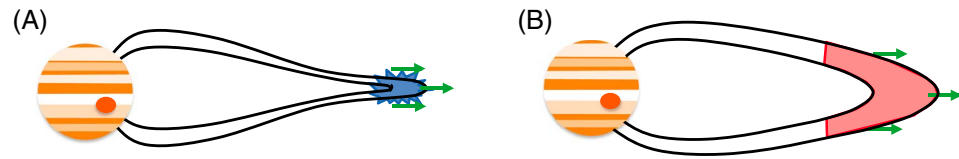
Figure 2. Schematic showing how heating due to rapid expansion of rotating flux tubes could result in a more dipolar field configuration and thicker current sheet. (a) Cold plasma is confined to the centrifugal equator. (b) As plasma heats, it moves farther off the equator, and the field dipolarizes.

For the case of a rotating plasma viewed in the rotating frame, particle energy gains or losses during adiabatic outward motion are more nuanced due to the effects of the centrifugal force. If the magnetic field is constant in time, one can define an energy constant C, given by

$$C \equiv \frac{m}{2}\left(v_\parallel^2 - \rho^2\Omega^2\right) + \mu B + q\phi \tag{3}$$

[*Northrop and Birmingham*, 1982]. Under adiabatic expansion, a particle will gain parallel energy as it moves to a larger ρ along the centrifugal potential (assuming very high conductivity in the ionosphere such that the plasma remains in corotation) but may lose some parallel energy to conserve J and will lose perpendicular energy to conserve μ as it moves to a weaker magnetic field. Thus, a particle's net energy gain or loss during outward adiabatic expansion depends on a variety of factors, including the particle's initial energy and pitch angle, the field geometry (which affects both perpendicular and parallel energy changes through conservation of μ and J, respectively), and the centrifugal energy $\frac{m}{2}\rho^2\Omega^2$. Because a rotating particle loses perpendicular energy and gains centrifugal potential as it moves to larger ρ during adiabatic expansion in a time stationary magnetic field, its pitch angle becomes more field-aligned. In general, for the particle energies and field models considered in this study, we expect adiabatic expansion of a rotating flux tube to result in a net decrease in energy and a more field-aligned pitch angle distribution. Additionally, because the net energy decreases and the effects of the centrifugal force, which confines particles to the equator, increases with increasing ρ, in the absence of pitch angle scattering, the particles considered here become further confined to the centrifugal equator.

3.2. Nonadiabatic Flux Tube Expansion: The Case for a Kinetic Simulation

According to the *Kivelson and Southwood* [2005] theory of plasma sheet thickening, flux tubes expand radially as they rotate from noon to dusk on time scales that are short compared to particle bounce periods, so the second adiabatic invariant is violated. Table 1 lists bounce periods that were calculated numerically for the initial configuration of the field model described in section 4.3. Estimates of the plasma temperature range from a few keV to tens of keV [*Goertz et al.*, 1979; *McNutt et al.*, 1981; *Kane et al.*, 1995, 1999], but even at the high end of the temperature range, typical bounce periods are several hours due to the large scale size of Jupiter's magnetosphere. For example, a 1 keV, 20 m_p particle in the middle magnetosphere has a bounce period of ~4–7 h, while for a 50 keV particle the bounce period is ~1–5 h. By comparison, the time scale for the field line stretching and rotation between noon and dusk is 5 h, assuming an azimuthal flow speed of half corotation. The resulting nonadiabatic behavior has important implications as to how the energy and pitch angle distributions evolve.

Consider, for example, two particles in the rotating frame with the same equatorial energy on a rotating flux tube, with particle 1 located at its mirror point at a distance ρ_m and particle 2 located at the equator at ρ_e. In general, the increase in centrifugal potential energy a particle experiences as a flux tube moves out from a distance ρ to $(\rho + \Delta\rho)$, with $\Delta\rho$ small compared with ρ, is proportional to $2\rho\Delta\rho + \Delta\rho^2 \approx 2\rho\Delta\rho$. If the field line stretches adiabatically, the net change in centrifugal potential energy (averaged over a bounce period) is the same for each particle and is proportional to the particles' average cylindrical distance during a bounce period. However, for nonadiabatic field line stretching, the increase in centrifugal potential energy differs for the two particles, which may lead to a net increase in energy during the nonadiabatic expansion. These points are illustrated in Figure 3, which shows how the position and energy of two sample particles evolve under both adiabatic and nonadiabatic expansions over a distance $\Delta\rho$. One particle begins at its mirror point (red line), and the other begins at the equator (black line), and in the absence of flux tube expansion these two particles would have the same energy and pitch angle at the equator. Figure 3 (top) shows the particles'

Table 1. Bounce Times for Particles of Mass 20 m_p, on a Stationary Field Line in the Rotating Frame [$\Omega = 2\pi/(20\,h)$], Starting With 100 eV–50 keV Energy at the Equator

Equatorial Energy	Equatorial Pitch Angle (deg)	Field Line Equatorial Crossing Distance (R_J)	Bounce Time (h)
100 eV	20	40	6.06
100 eV	40	40	5.89
100 eV	60	40	5.70
100 eV	80	40	5.59
1 keV	20	30	9.39
1 keV	40	30	7.13
1 keV	60	30	5.62
1 keV	80	30	4.92
1 keV	20	40	7.57
1 keV	40	40	6.03
1 keV	60	40	4.80
1 keV	80	40	4.20
1 keV	20	50	6.49
1 keV	40	50	5.41
1 keV	60	50	4.43
1 keV	80	50	3.92
10 keV	20	40	9.00
10 keV	40	40	4.59
10 keV	60	40	2.49
10 keV	80	40	1.82
50 keV	20	40	4.47
50 keV	40	40	2.69
50 keV	60	40	1.28
50 keV	80	40	0.85

positions in a meridian plane. In Figure 3 (top left) the expansion proceeds adiabatically, so the particles complete several bounce periods as the flux tube expands. By comparison, during the much faster nonadiabatic expansion shown in the Figure 3 (top right), the particles do not complete a bounce period. Figure 3 (bottom) shows the particles' energy as a function of time (black and red lines); the two particles begin with different energy because they are different positions along the centrifugal potential. The time axis in Figure 3 (bottom) is scaled so that both the adiabatic (left) and nonadiabatic (right) panels show the amount of time required for the flux tube to expand over a distance $\Delta\rho$. Periodic fluctuations in the adiabatic panel occur over a bounce period; fluctuations in the nonadiabatic panel occur over a gyroperiod. The average energy of the two particles in the nonadiabatic case initially decreases but then increases and remains at a higher level than the adiabatic case.

An energy constant equivalent to that given in equation (3) cannot be defined if the second adiabatic invariant is violated due to rapid flux tube expansion, as occurs in Jupiter's magnetosphere between noon and dusk, or if the magnetic field is not constant in time, as is the case for the field models we use in the simulation (see section 4.3). Therefore,
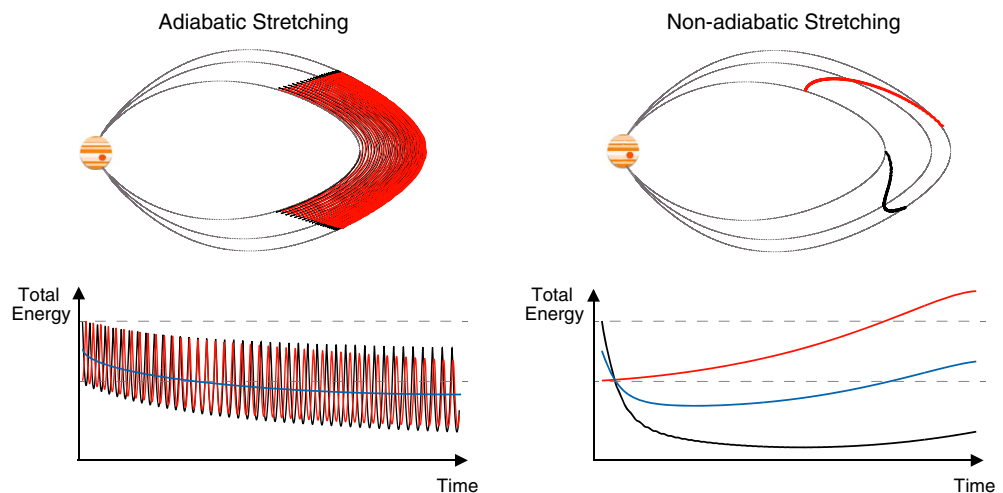

Figure 3. Illustration showing how nonadiabatic expansion can lead to an increase in total energy. (top) A meridian plane view of two example particle orbits as a rotating flux tube expands (left) adiabatically and (right) nonadiabatically over a distance $\Delta\rho$. One particle begins at the equator (black line), and the other begins at its mirror point (red line). Both particles have the same initial equatorial energy and pitch angle in the absence of flux tube expansion. Dashed gray lines show sample field lines during expansion. (bottom) The particles' energy versus time, with black indicating the initially equatorial particle and red indicating the initially mirroring particle. The blue line in Figure 3 (bottom left) shows the bounce-averaged energy of the two particles, and the blue line in Figure 3 (bottom right) shows the average energy of the two particles. The time axis in the bottom panel has been scaled so that both panels show the time required for the flux tube to expand over a distance $\Delta\rho$ (much longer for the adiabatic expansion).

we cannot analytically determine how the particle energy and pitch angle distributions evolve in response to the flux tube expansion and must instead track particles by solving their equations of motion, as is done numerically in a large-scale kinetic simulation.

4. Methods: An LSK Model

4.1. Overview and Purpose of the Simulation

We have used a large-scale kinetic (LSK) model [*Ashour-Abdalla et al.*, 1993] to create a "toy" problem wherein we follow particles on one expanding flux tube to study how the energy and pitch angle distributions change in a system designed to mimic the properties of the field in the Jovian noon-to-dusk magnetosphere. Jupiter's magnetopause flares between noon and dusk, so that the equatorial crossing points of flux tubes rotating through this local time sector move outward by as much as 50% of their location at noon, and the flux tube volumes increase. In our simulation we represent this process by modeling an axially symmetric flux tube in the rotating frame that stretches over distance and time scales representative of the flux tube expansion observed between noon and dusk in Jupiter's magnetosphere.

The combined effects of the centrifugal force and rapid field line stretching influence the particle energy and pitch angle distributions over time. However, we must compare the end distributions not just to the initial values but also to the distributions evolved under adiabatic expansion. Therefore, we have tracked particles on an expanding flux tube for two different cases: one with a slow (500 h) adiabatic time scale and one with a much faster (5 h) stretching time scale in which the second adiabatic invariant is violated. The time scale for the rapid expansion was chosen to correspond to the time required for flux tubes to rotate between noon and dusk in Jupiter's magnetosphere, assuming an azimuthal motion at half corotation, which is consistent with the subcorotational flow velocities observed in the middle magnetosphere [*Belcher*, 1983; *Krupp et al.*, 2001]. The adiabatic results serve as a baseline for comparison with the nonadiabatic run. In both cases, we load particles with the same initial energy and pitch angle distributions on a representative flux tube with an initial 40 R_J equatorial crossing distance; this distance increases to ~55 R_J as the field line stretches. The selected initial crossing distance lies well within both the compressed (~60 R_J) and uncompressed (~90 R_J) magnetopauses at noon. It also is sufficiently large such that over a 5 h interval, its outward displacement (to ~55 R_J) covers a significant distance. Expansion from $\rho = 40\,R_J$ to $\rho = 55\,R_J$ represents an increase of ~23 keV of centrifugal potential energy, though any net increase in energy will be reduced through betatron acceleration as the field magnitude decreases.

4.2. Setup of an LSK Analysis

An LSK approach rather than a magnetohydrodynamic simulation is required for our purposes because the effects of flux tube expansion depend on the initial energy, pitch angle, and position along a flux tube of the plasma particles. Furthermore, for most particles in the energy range of interest, the second adiabatic invariant J is not conserved during the outward expansion. LSK models integrate particle orbits by solving the particle equation of motion, or the Lorentz force equation, which takes the form

$$m\frac{d\mathbf{v}(t)}{dt} = q(\mathbf{E}(t) + \mathbf{v}(t) \times \mathbf{B}(t)) - m(2\mathbf{\Omega} \times \mathbf{v}(t) + \mathbf{\Omega} \times \mathbf{\Omega} \times \mathbf{r}) \tag{4}$$

in the rotating frame [*Birmingham and Northrop*, 1979]. Here $\mathbf{v}(t)$ is the particle's velocity in the rotating frame, and $\mathbf{E}(t)$ and $\mathbf{B}(t)$ are specified global electric and magnetic fields, respectively, that may be functions of time. The electric and magnetic field models used in this simulation are presented in section 4.3. We use a fourth-order Runge-Kutta method, a common approach to solving differential equations numerically. The LSK code used in this simulation was written specifically for this study.

For the analysis of the combined effects of rotation and a changing magnetic field, one must include three sources of the electric field in the inertial frame. The first is the corotation electric field, $(\mathbf{r} \times \mathbf{\Omega}) \times \mathbf{B}$; in the rotating frame, this term vanishes. The second contribution to the electric field is the induction electric field that arises from time variations of the magnetic field:

$$\nabla \times \mathbf{E} = -\frac{\partial \mathbf{B}}{\partial t}. \tag{5}$$

The electric field could include a further contribution from a scalar potential ϕ, where $\mathbf{E}_{\text{potential}} = -\nabla\phi$; however, we assume that only the induction electric field need be considered in the rotating frame.

We work in the rotating frame because it is very close to the rest frame of the plasma (neglecting gradient and curvature drifts, which are small) in the absence of the motion associated with field stretching. The induction electric field used to stretch the field produces a guiding center drift velocity:

$$\mathbf{v}_D = \frac{\mathbf{E}_{induction} \times \mathbf{B}}{B^2}. \tag{6}$$

This must be accounted for when determining a particle's thermal energy, which is defined with respect to the (drifting) guiding center. Additionally, we drop the term in equation (4) associated with the Coriolis force, $-2m(\mathbf{\Omega} \times \mathbf{v})$, and retain only the component of the centrifugal force that is parallel to **B** so that the final equation of motion solved in the LSK simulation is

$$m\frac{d\mathbf{v}(t)}{dt} = q(\mathbf{E}(t) + \mathbf{v}(t) \times \mathbf{B}(t)) - m(\mathbf{\Omega} \times \mathbf{\Omega} \times \mathbf{r}) \cdot \hat{b}, \tag{7}$$

where $\hat{b}$ is a unit vector along the magnetic field. Dropping the Coriolis force term is justified because its effect on an outward moving plasma is to produce a drift opposite to the rotational flow direction, which would bend the field line. This effect is independent of particle energy. We assume that ionospheric conductivity is high enough that particles remain fully corotational but neglect the magnetopause currents or magnetic tension which would provide a restoring force to straighten the field line and maintain rigid rotation. As this magnetic effect would counter the displacement arising from the Coriolis force, we drop the Coriolis force for consistency. Similarly, we neglect the component of the centrifugal force perpendicular to **B** because its effect is to produce an azimuthal drift. This drift depends on ρ (though, like the Coriolis force, it is independent of particle energy) but does not affect the particle energy in the guiding center frame. Therefore, it can be ignored because complete azimuthal symmetry is assumed. Finally, we assume the field lines are rigidly rotating with a rotation period of 20 h, half of Jupiter's rotation period, which is consistent with the observed subcorotational flow velocities [*Belcher*, 1983; *Krupp et al.*, 2001].

4.3. Electric and Magnetic Field Models

We represent Jupiter's magnetic field by a simplified, axisymmetric, and time-varying model developed from the *Khurana* [1997] field. The field axis is aligned with the spin axis, and the centrifugal and jovigraphic equators are collocated. The field lines are taken to lie in meridian planes with no bendback. This field can be derived from two scalar stream functions, f and g, such that

$$\mathbf{B} = \nabla f \times \nabla g \tag{8}$$

which assures that **B** is divergence free. The Euler potentials f and g are constant along a field line. The field is constructed according to the following stream functions:

$$f(\rho, \varphi, z, t) = M_J \frac{\rho^2}{(\rho^2 + z^2)^{3/2}} - C_1(t)\rho \left(\tanh \frac{r_{01}(t)}{r} \right)^{A_1} \ln \cosh \frac{z}{D_1} - \frac{A(t)}{B(t)^2} e^{-\rho B(t)} (\rho B(t) + 1)$$

$$- \frac{C(t)}{D(t)^2} e^{-\rho D(t)} (\rho D(t) + 1) - \frac{E(t)}{F(t)^2} e^{-\rho F(t)} (\rho F(t) + 1) + \frac{\rho^2 G(t)}{2}$$

$$g(\rho, \varphi, z, t) = \varphi. \tag{9}$$

Here ρ, φ, and z define the cylindrical coordinate system, M_J is the dipole moment, A_1 and D_1 are constants, and the remaining terms ($C_1(t)$, $A(t)$, $B(t)$, etc.) vary linearly with time. The first term in the stream function f contains the contributions of the dipole field, while the remaining terms contain the field stretching due to the current sheet, which varies in time.

The stream functions in equation (9) are simplified and modified from the *Khurana* [1997] field. The Khurana model was fit to data from the midnight to dawn local time sector, where field lines are more radially stretched than at noon. Therefore, we altered the values of some variables (A_1, D_1, $C_1(t)$, $A(t)$, etc.) to better match the observed field configuration near noon. In the absence of rotation, this change of model values also ensures adiabatic bounce motion and conservation of μ in our energy range of interest by increasing the
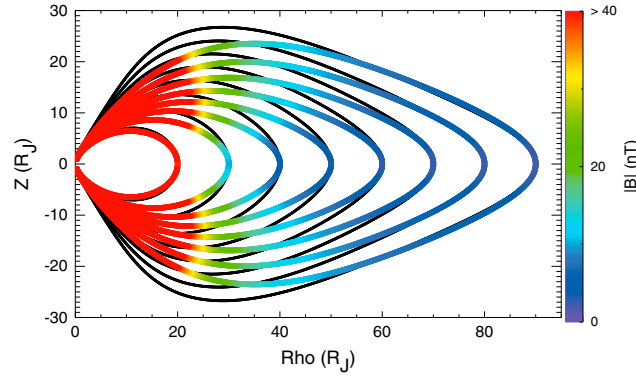
Figure 4. Model magnetic field configuration, shown in a meridional plane. The colored lines show the initial configuration, with the color indicating the field magnitude, while the black lines show the field configuration after 5 h for the nonadiabatic case (or 500 h for the adiabatic case) with field lines draw from the same equatorial crossing points. See Figure 5 for an illustration of how the initial field lines stretch over time for the rapid expansion case.

field line radius of curvature. (Adiabatic motion requires $\kappa^2 \gg 1$, where κ is the ratio of the radius of curvature to the gyroradius [*Büchner and Zelenyi*, 1989].) We also added a time dependence to the original Khurana model and altered the form of the stream function f (specifically, the third through fifth terms) so that the time derivative can be explicitly evaluated to determine the induction electric field (see equation (14) below).

From equations (8) and (9), the field can be written as

$$\mathbf{B} = \left\{ -\frac{1}{\rho} \frac{\partial f}{\partial z}, 0, \frac{1}{\rho} \frac{\partial f}{\partial \rho} \right\} \quad (10)$$

so that the components of the magnetic field in cylindrical coordinates are

$$B_\rho(t) = \frac{3M_J \rho z}{r^5} - C_1(t) A_1 r_{01}(t) \frac{z}{r^3} \left(\tanh \frac{r_{01}(t)}{r} \right)^{A_1 - 1} \left[\operatorname{sech} \frac{r_{01}(t)}{r} \right]^2 \ln \cosh \frac{z}{D_1}$$

$$+ \frac{C_1(t)}{D_1} \left(\tanh \frac{r_{01}(t)}{r} \right)^{A_1} \tanh \frac{z}{D_1}$$

$$B_\varphi = 0$$

$$B_z(t) = \frac{M_J(2z^2 - \rho^2)}{r^5} + C_1(t) A_1 r_{01}(t) \frac{\rho}{r^3} \left(\tanh \frac{r_{01}(t)}{r} \right)^{A_1 - 1} \left[\operatorname{sech} \frac{r_{01}(t)}{r} \right]^2 \ln \cosh \frac{z}{D_1}$$

$$- \frac{C_1(t)}{\rho} \left(\tanh \frac{r_{01}(t)}{r} \right)^{A_1} \ln \cosh \frac{z}{D_1} + A(t) e^{-\rho B(t)} + C(t) e^{-\rho D(t)} + E(t) e^{-\rho F(t)} + G(t). \quad (11)$$

The resulting field is shown in Figure 4.

The induction electric field must be consistent with the time variations in the magnetic field to satisfy equation (5). The magnetic field can be written as the curl of a vector potential **A**, implying that

$$\mathbf{B} = \nabla \times \mathbf{A} = \nabla \times (f \nabla g) \quad (12)$$

and

$$\mathbf{A} = f \nabla g = \frac{f}{\rho} \hat{\varphi}. \quad (13)$$

Then, by equation (5)

$$\mathbf{E}_{\text{induction}} = -\frac{\partial \mathbf{A}}{\partial t} = -\frac{1}{\rho} \frac{\partial f}{\partial t} \hat{\phi}. \quad (14)$$

The temporal variations in the magnetic field model were designed to reproduce two main observed features of the field changes from noon to dusk. The first observed feature is that the equatorial crossing points of all flux tubes move radially outward by as much as ~35 R_J from noon to dusk as the magnetopause distance increases from ~63 R_J at noon to ~85 R_J at dusk in the compressed case or from ~92 R_J at noon to ~127 R_J at dusk in the expanded case [*Joy et al.*, 2002]. In our time-varying model, a flux tube with an initial equatorial distance of 60 R_J expands radially outward to ~80 R_J, and a flux tube initially at 90 R_J expands to ~126 R_J. The second feature is that the field is more dipolar (i.e., has a larger radius of curvature) at dusk than at noon, as seen by comparing the initial (colored lines) and final (black lines) model field configurations in Figure 4. Figure 5a shows a meridian plane view of a single flux tube that starts with an equatorial crossing at 40 R_J at noon and expands to its final equatorial crossing at ~55 R_J over 5 h for the nonadiabatic stretching case or
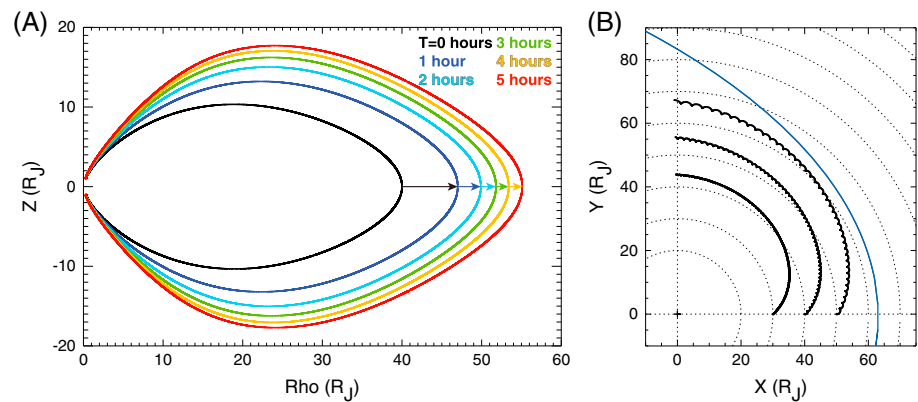
Figure 5. (a) Time evolution of a model field line starting with an equatorial crossing distance of 40 R_J then stretching radially outward to 55 R_J over 5 h for the nonadiabatic stretching case or 500 h for the adiabatic stretching case. (b) Evolution of three example 90° pitch angle particles in the equatorial plane showing outward motion from noon to dusk. Particle orbits are shown in black, and the compressed magnetopause location from *Joy et al.* [2002] is shown in blue. The Sun is to the right.

500 h for the adiabatic stretching case. Figure 5b shows an equatorial plane view of three sample trajectories for equatorial particles with 90° pitch angles, starting at noon at 30, 40, and 50 R_J. The figure shows the particle motion in the nonrotating frame to illustrate the azimuthal motion from noon to dusk and the outward expansion.

4.4. Model Limitations

The simplifying assumptions made in our simulation (e.g., using an axially symmetric magnetic field model and simulating particle properties on just one representative flux tube) reduce our computing requirements to a realistic level and allow us to isolate the two processes, nonadiabatic flux tube expansion and rapid rotation, that are relevant to our study. However, our model also has some significant limitations and is not fully self-consistent. In loading the flux tube (see section 4.6 below) we do not require balance between the forces exerted by the plasma particles and magnetic pressure and the curvature force. In later time steps, we do not allow the plasma to influence the magnetic field geometry, nor do we consider instabilities that may affect the particle distributions. Among other implications, this means that we do not model pitch angle scattering even if the distribution function is anisotropic. Since the time scale for pitch angle scattering is short (approximately one quarter of a bounce period or shorter) [*Treumann and Baumjohann*, 2001], we would expect some pitch angle scattering to occur even during the 5 h time scale for rapid flux tube expansion. Therefore, the pitch angle anisotropy that exists at the end of our simulation run is likely an overestimate, since at least some of the distribution would have reisotropized through pitch angle scattering.

4.5. Tests of Accuracy

The code used in this simulation was modeled after an existing LSK code [e.g., *Ashour-Abdalla et al.*, 1993] but was written specifically for this work. Accuracy is of particular concern when developing new code, so wherever possible we tested our results for both numerical and physical accuracy. For example, using a few dozen test particles with a range of initial positions, energies, and pitch angles, we confirmed that our Runge-Kutta method conserves particle energy, μ, and J on nonrotating flux tubes to at least five significant figures. We also confirmed that the calculated particle energy and bounce motion on a stationary flux tube in the rotating frame proceeds according to our physical expectations (as outlined in Appendix A). We thoroughly tested our method of field line expansion to ensure that the outward drift velocity is consistent with the induction electric field and time variations in the magnetic field model and that μ is still conserved in the expanding field. We confirmed numerically that the second adiabatic invariant is not conserved when the field line expansion time scale is only 5 h but is conserved for a 500 h stretching time scale.

4.6. Distribution of Particles Along the Initial Flux Tube

We loaded the field lines with particles representing physically reasonable velocity space distributions along a flux tube with an initial 40 R_J equatorial crossing distance. Selecting an appropriate initial distribution function was a crucial step because flux tube expansion acts differently on particles depending on their initial energy, position, and pitch angle. Starting with a time-independent magnetic field in the rotating frame,

we imposed the requirement that the initial particle distribution at each point along the flux tube must remain constant as the particles bounce up and down. This implies that changes to the pitch angle or energy distribution in later analyses using a time-varying field can be attributed to the effects of outward expansion.

In a time-independent field and in the absence of rotation, an isotropic Maxwellian with a constant density along the flux tube is a time stationary solution. However, we know that the outward directed centrifugal force opposes inward motion and modifies the form of a steady state distribution function for plasma on a rotating flux tube. Given an equatorial distribution function f, the steady state distribution function at an arbitrary point (ρ, z) along the field line can be found by solving the Vlasov equation

$$\frac{\partial f}{\partial t} + \mathbf{v} \cdot \nabla_{\vec{x}} f + \mathbf{F} \cdot \nabla_{\vec{v}} f = 0 \tag{15}$$

assuming that the time derivative vanishes. For a rotating system, the force $\mathbf{F}$ includes both the Lorentz and centrifugal forces. This approach was used by *Huang and Birmingham* [1992] to derive the density along a rotating flux tube given a bi-Maxwellian distribution at the equator. One may instead assume an isotropic Maxwellian distribution at the equator

$$f(v) = A e^{-\frac{mv^2}{2kT}}, \tag{16}$$

where k is the Boltzmann constant, T is temperature, and the constant $A = n_0 \left(\frac{m}{2\pi kT}\right)^{3/2}$, where n_0 is the equatorial density. Solving equation (15) for the distribution function at an arbitrary point (ρ, z) on the field line we find

$$f(\rho, z, v) = A e^{-\frac{mv^2}{2kT}} e^{\frac{m(\rho^2 - \rho_e^2)\Omega^2}{2kT}}, \tag{17}$$

where ρ_e is the field line's cylindrical radial distance at the equator. This expression reduces to the result of *Huang and Birmingham* [1992] if $T = T_{//} = T_\perp$.

The density at a point (ρ, z) on the field line is found by integrating $f(\rho, z, v)$ over velocity, which yields

$$n(\rho) = n_0 e^{\frac{m(\rho^2 - \rho_e^2)\Omega^2}{2kT}}. \tag{18}$$

The density falloff away from the equator depends on both Ω and kT in such a way that equatorial confinement of plasma increases with increasing rotation rate and decreasing temperature. Hot plasma would be able to overcome the effects of the centrifugal force and fill the flux tube more uniformly than cooler plasma. Equation (18) reduces to the familiar exponential scale height relationship for a rotating system [*Gledhill*, 1967; *Hill and Michel*, 1976; *Bagenal and Sullivan*, 1981; *Vasyliūnas*, 1983] for a dipole field near the equator.

Equations (17) and (18) describe how the distribution function and density vary along a field line given an equatorial Maxwellian distribution. At Jupiter, ions are better described by a kappa distribution [*Krimigis et al.*, 1981] defined as

$$f(v) = A_\kappa \left[1 + \frac{\frac{1}{2}mv^2}{\kappa E_s}\right]^{-\kappa-1}, \tag{19}$$

where E_s is the characteristic energy of the distribution and $A_\kappa = n_0 \frac{m}{2\pi(\kappa E_s)^{3/2}}$ [*Vasyliūnas*, 1968]. The kappa distribution is similar to a Maxwellian at low energy and a power law at high energy. The constant κ represents the relative weighting of the high- and low-energy parts of the distribution, and as $\kappa \to \infty$, the distribution function becomes a Maxwellian. Again, invoking the Vlasov equation, we find that the distribution function at a point (ρ, z) on the field line is

$$f(\rho, z, v) = A_\kappa \left[1 + \frac{\frac{1}{2}mv^2 - \frac{1}{2}m\Omega^2(\rho^2 - \rho_e^2)}{\kappa E_s}\right]^{-\kappa-1}, \tag{20}$$

and the density along the field line is given by

$$n(\rho) = n_0 \left(1 - \frac{m(\rho^2 - \rho_e^2)\Omega^2}{2\kappa E_s}\right)^{-\kappa+1/2} \tag{21}$$
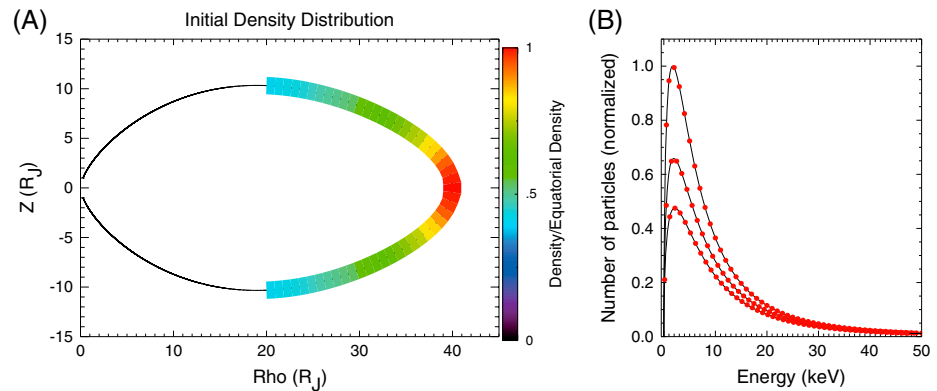
[*Pierrard and Lemaire*, 1996].

Figure 6. Initial density and energy distribution of the particles launched in the simulation along the field line that crosses the equator at 40 R_J. (a) The initial density distribution along the field line. (b) The initial distribution function (equation (20)) as a function of energy, at three distances along the field line corresponding to $\rho = 30$, 35, and 40 R_J; the red dots indicate the energies at which particles were launched. The three curves have different peak values because the density decreases with distance along the field line.

Using equations (17) and (20) to determine the relative numbers of particles to place at all initial positions (ρ, z) and energies ($\frac{1}{2}mv^2$), we tested the stability of our initial distribution by tracking the particles, in the rotating frame, through their bounce motion along a rotating flux tube to see if significant changes developed in the pitch angle or energy distributions in the absence of flux tube expansion. For the initial distribution, we placed particles every 0.1 R_J along the initial field line, from the equatorial crossing point at 40 R_J inward to an inner cutoff at $\rho = 20$ R_J, having verified that the number of particles within this distance was negligible compared to those at the equator. In order not to lose particles from the simulation, we placed a reflecting boundary at 18 R_J, such that any particle whose bounce motion took it to 18 R_J was reflected back with the same energy and supplementary pitch angle. Particles were launched at random gyrophases, in 101 pitch angle bins of equal $d(\cos \alpha)$, and with equatorial energies ranging from 500 eV to 50 keV (in bins of 1 keV from 1 to 50 keV). In all, we tracked more than 2 million particles for this initial test and for both the adiabatic and nonadiabatic expansion runs.

The parameters of the initial distribution were selected after consulting published data. Reports of the plasma temperatures in Jupiter's middle magnetosphere vary by more than an order of magnitude. Some early measurements suggested a ~1–2 keV Maxwellian [*Goertz et al.*, 1979; *McNutt et al.*, 1981], while *Krimigis et al.* [1981] showed that at Jupiter, ions follow a kappa distribution [*Vasyliūnas*, 1968], which approximates a Maxwellian with ~20–50 keV temperature at low energy and a power law at high energy. More recent data from Galileo's Plasma Subsystem [*Frank et al.*, 1992], which measured particles with energy per change of 0.9 V to 52 kV, suggested temperatures of ~4–8 keV [*Frank and Paterson*, 2002, 2004]. *Kane et al.* [1995, 1999] estimated a kappa distribution ($\kappa = 2$–4) with an even higher mean energy, ~20–80 keV, though that analysis was based on data from Galileo's EPD [*Williams et al.*, 1992], which measured ions with energies 20 keV and above, rather than the low-energy core of the distribution. The higher-energy part of the distribution dominates the energy density but not the number density, while the bulk plasma falls in the quasi-Maxwellian part of the distribution. Therefore, we focus on energies ranging from 500 eV to 50 keV for this simulation. We assume an equatorial kappa distribution with $\kappa = 3$ and $E_s = 4$ keV, which is the initial distribution used to obtain Figure 6 and used in the analysis presented in section 5. Given the large amount of variation in the temperature estimates, in section 6.2 we consider how the simulation results change for other initial parameters.

The initial density distribution along the field varies according to equation (21) and is plotted in Figure 6a. The density is highest at the equator and falls to ~40% of the equatorial value at our inner boundary ($\rho = 20$ R_J). Figure 6b shows the initial energy distribution of particles at three points along the field line ($\rho = 30$, 35, and 40 R_J). At all three positions the initial energy distribution is a 4 keV kappa distribution, but the number of particles decreases with distance along the field line away from the equator following equation (20).
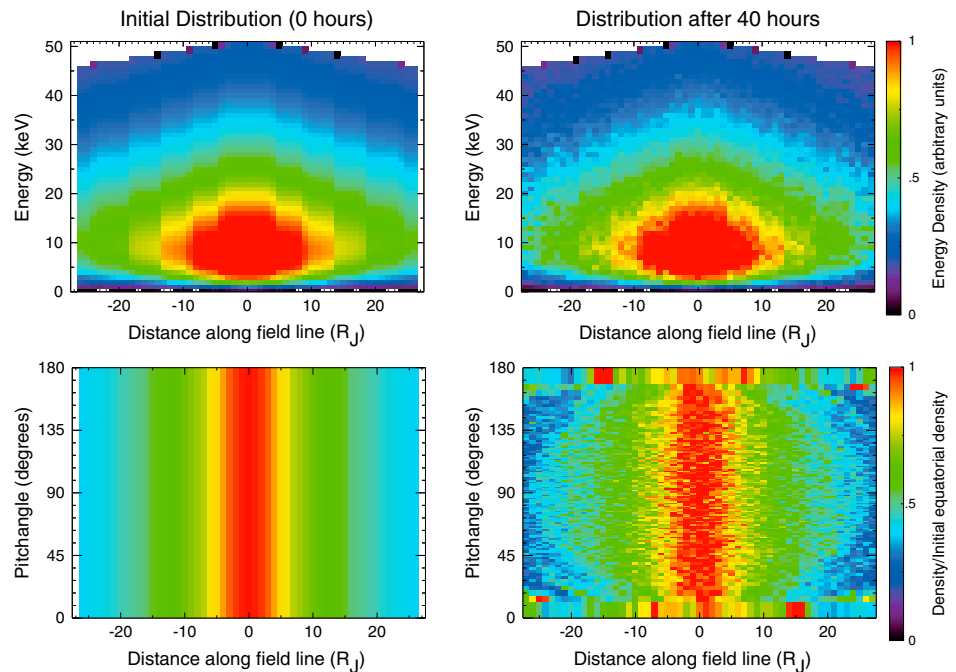
Figure 7. (top) Energy density and (bottom) pitch angle distributions at times (left) 0 and (right) 40 h in a rotating system, plotted versus distance along the field line (defined as 0 at the equator and positive northward). The computations include the centrifugal force in a static (nonstretching) magnetic field. The initial distribution, nominally steady state as described in section 4.6, is an isotropic 4 keV kappa distribution. The energy distribution, in Figure 7 (top left), is integrated over all pitch angles, and the pitch angle distribution is integrated over all energies. The distribution remains essentially constant over several bounce periods. A spurious density enhancement at 90° ± 1°, which appeared due to binning, has been removed from the initial pitch angle distribution plot here and in Figures 9 and 12.

Stability tests showed that in the absence of field line expansion, the energy, density, and pitch angle distributions along a rotating flux tube varied little over more than 40 h (several bounce periods, even for the slowest particles), as shown in Figure 7. Figure 7 (left) shows the initial energy density (top) and pitch angle (bottom) distributions, while Figure 7 (right) shows the respective distributions 40 h later. For the energy density distribution, we integrated over all pitch angles, and for the pitch angle distribution, we integrated over all energies. The distributions are plotted versus distance along the field line, which is defined as 0 at the equator and positive northward. The differences between the initial and final distributions in Figure 7 are negligible compared to the dramatic changes in the pitch angle and energy distributions in analogous plots during flux tube expansion (see discussion and figures in section 5). The anomalous behavior at the most field aligned pitch angles here and in subsequent pitch angle plots is likely due to poor statistics or rounding errors; similarly, anomalous horizontal bars near 90° in later pitch angle plots are due to binning and rounding errors. We are therefore reasonably confident that our choice of initial distribution represents the steady state distribution in the rotating frame in the absence of any field line expansion and that the changes discussed in the next section are due to the effects of flux tube expansion.

5. Results: Properties of the Particle Distribution on a Stretching Flux Tube

Using the LSK simulation and the initial distribution of particles outlined in section 4, we launched more than 2 million particles with mass 20 m_p and tracked their motion through the time-dependent magnetic field model under both adiabatic and nonadiabatic flux tube expansions. In the following subsections we show how the energy, pitch angle, and spatial distributions evolved for each case.

5.1. Pitch Angle and Energy Evolution Under Adiabatic Stretching

As discussed in section 3.1, following adiabatic expansion of a rotating flux tube we expect that the pitch angle distribution will become more field-aligned, particles will be increasingly confined to the centrifugal equator, and the total energy will decrease due to conservation of μ and J. The distributions of position,
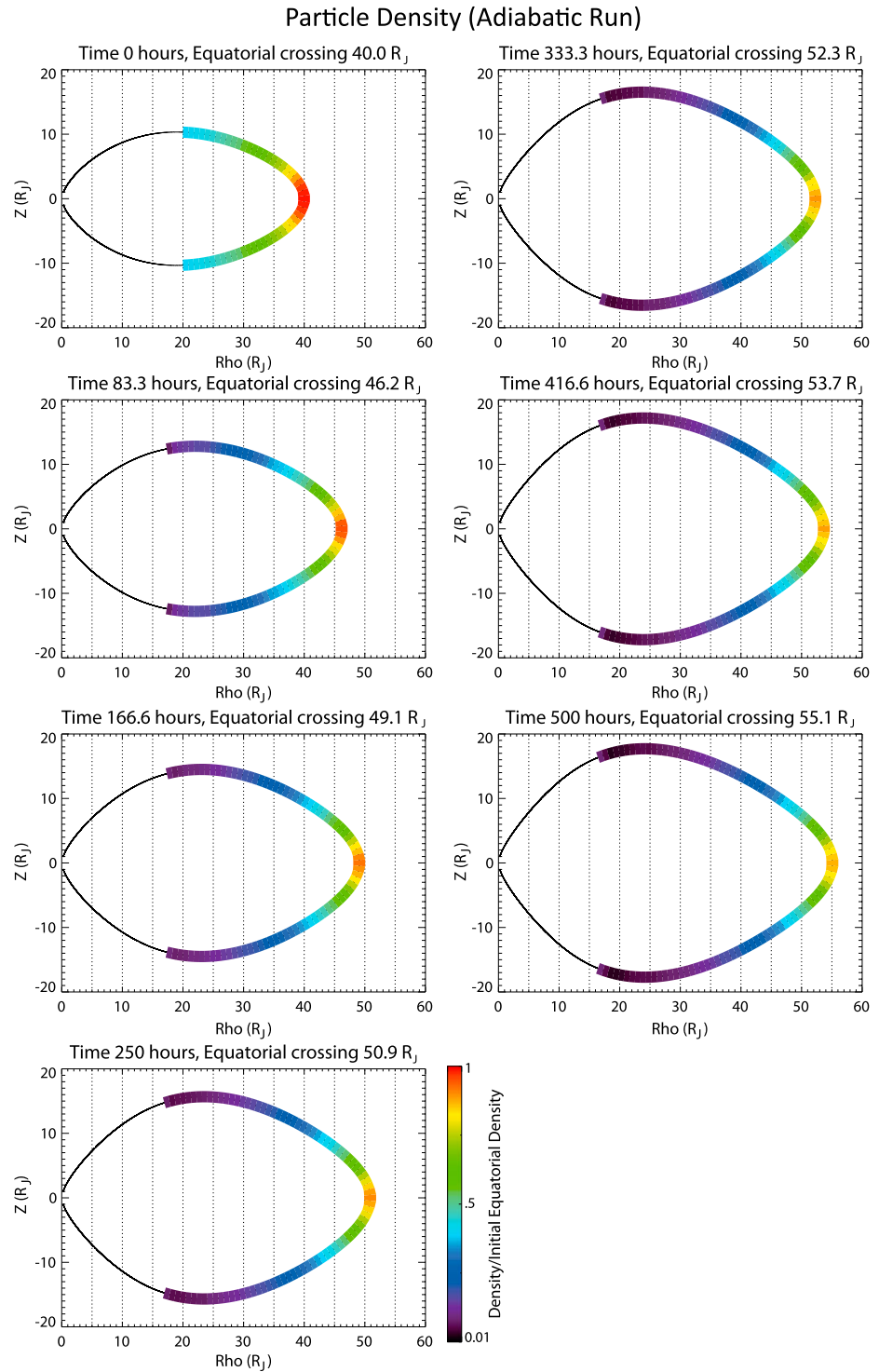
Figure 8. Time evolution of density along the field line for the adiabatic, or slow stretching case (initial 4 keV kappa distribution), in which the field line's equatorial crossing point moves outward from 40 R_J to ~55 R_J over 500 h. Color indicates density, in bins of equal distance along the field line, relative to the initial density at the equator. Vertical dashed lines are drawn every 5 R_J to guide the eye.

density, pitch angle, and energy density shown in Figures 8–10 evolve qualitatively as expected. Figure 8 shows the density distribution along the flux tube at selected times during the outward displacement normalized to the initial equatorial density. Particles are increasingly confined to the equator as the flux tube moves out. Because the flux tube volume increases as it moves out (the cross-sectional area increases like 1/B,

Pitch Angle Distribution (Adiabatic Run)
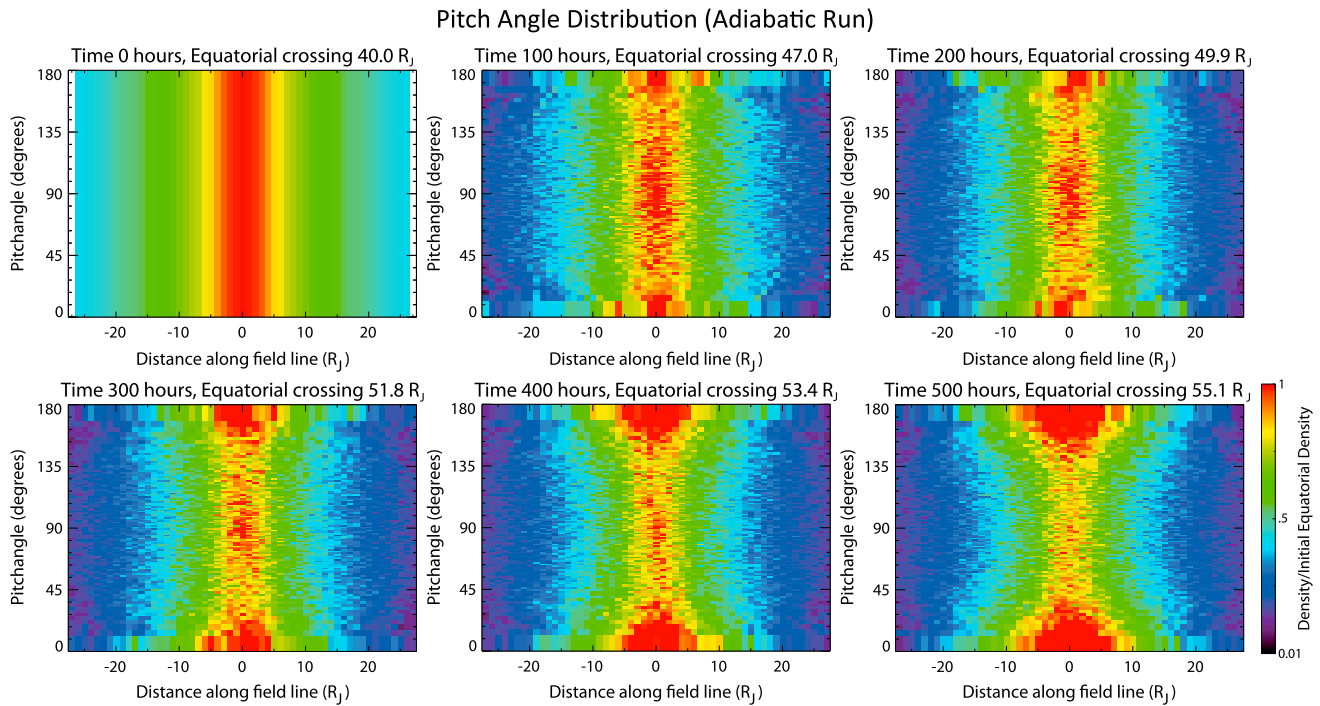
Figure 9. Pitch angle distribution for the adiabatic stretching case (initial 4 keV kappa distribution), shown here as a function of distance along the field line, following the format of the Figure 7 (bottom). Color indicates the density of particles within pitch angle bins of constant size $d(\cos\alpha)$. The initial distribution consists of vertical color bands corresponding to the initial isotropic distribution. As the flux tube stretches outward, the distribution becomes more field-aligned, especially near the equator.
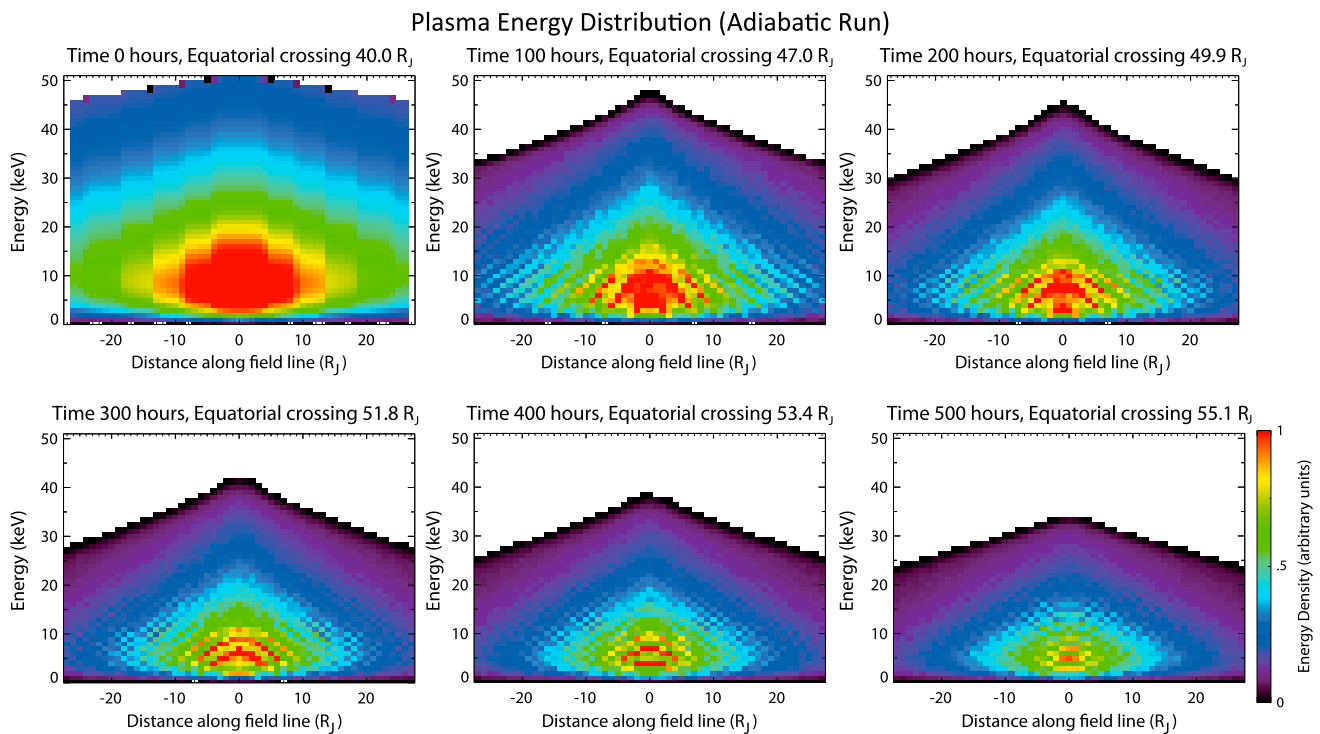
Plasma Energy Distribution (Adiabatic Run)

Figure 10. Time evolution of the plasma energy distribution as a function of distance along the field line, for the adiabatic stretching case, following the format of Figure 7 (top). The initial distribution consists of a 4 keV kappa distribution at all points along the field line, with the density decreasing with distance along the field line (see equation (21)). As the flux tube expands radially outward, the energy decreases everywhere along the field line.
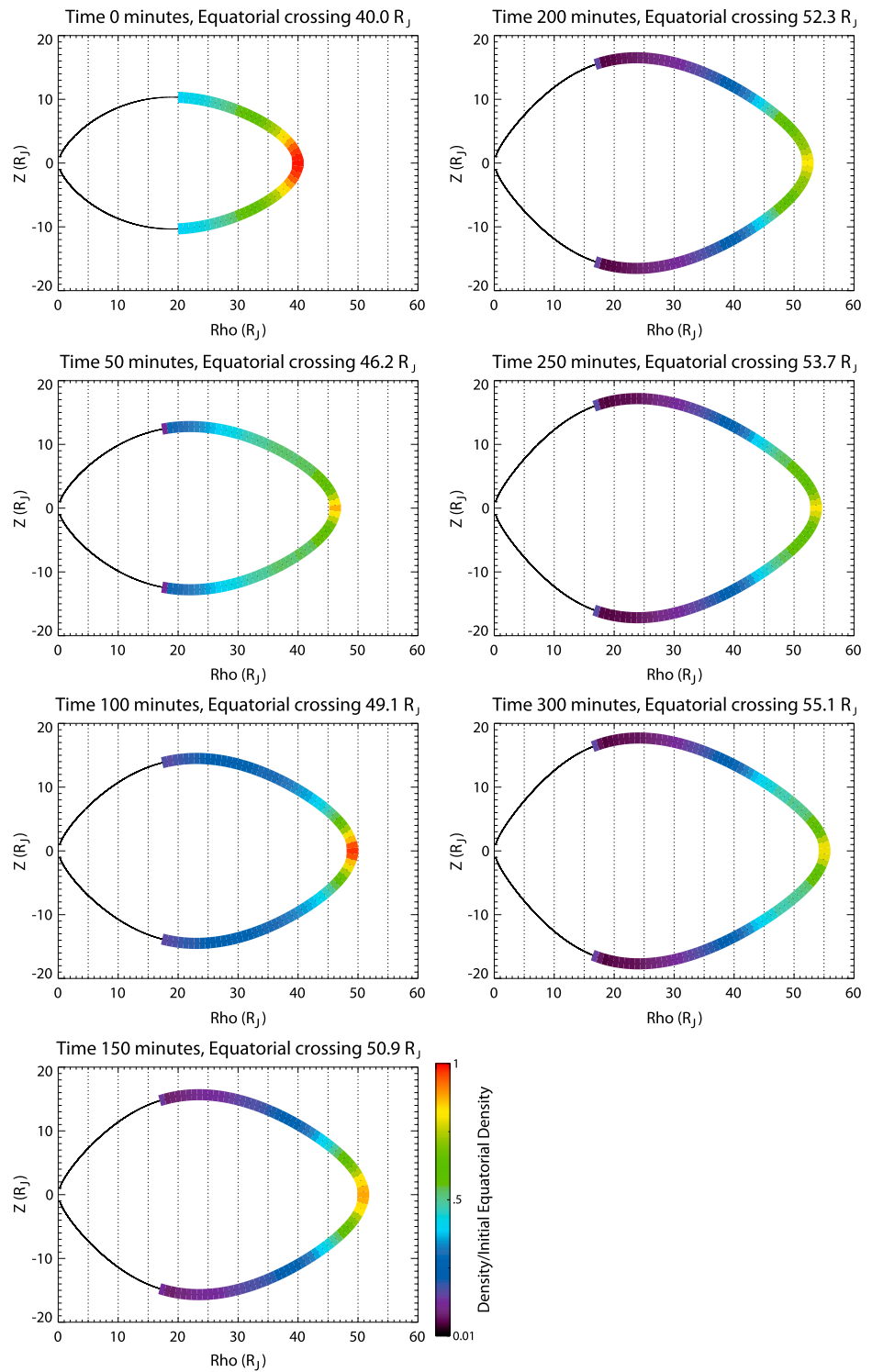
Figure 11. As in Figure 8 but for the nonadiabatic, or fast stretching, case (initial 4 keV kappa distribution). Here the field line expansion from 40 R_J to ~55 R_J occurs in 5 h.
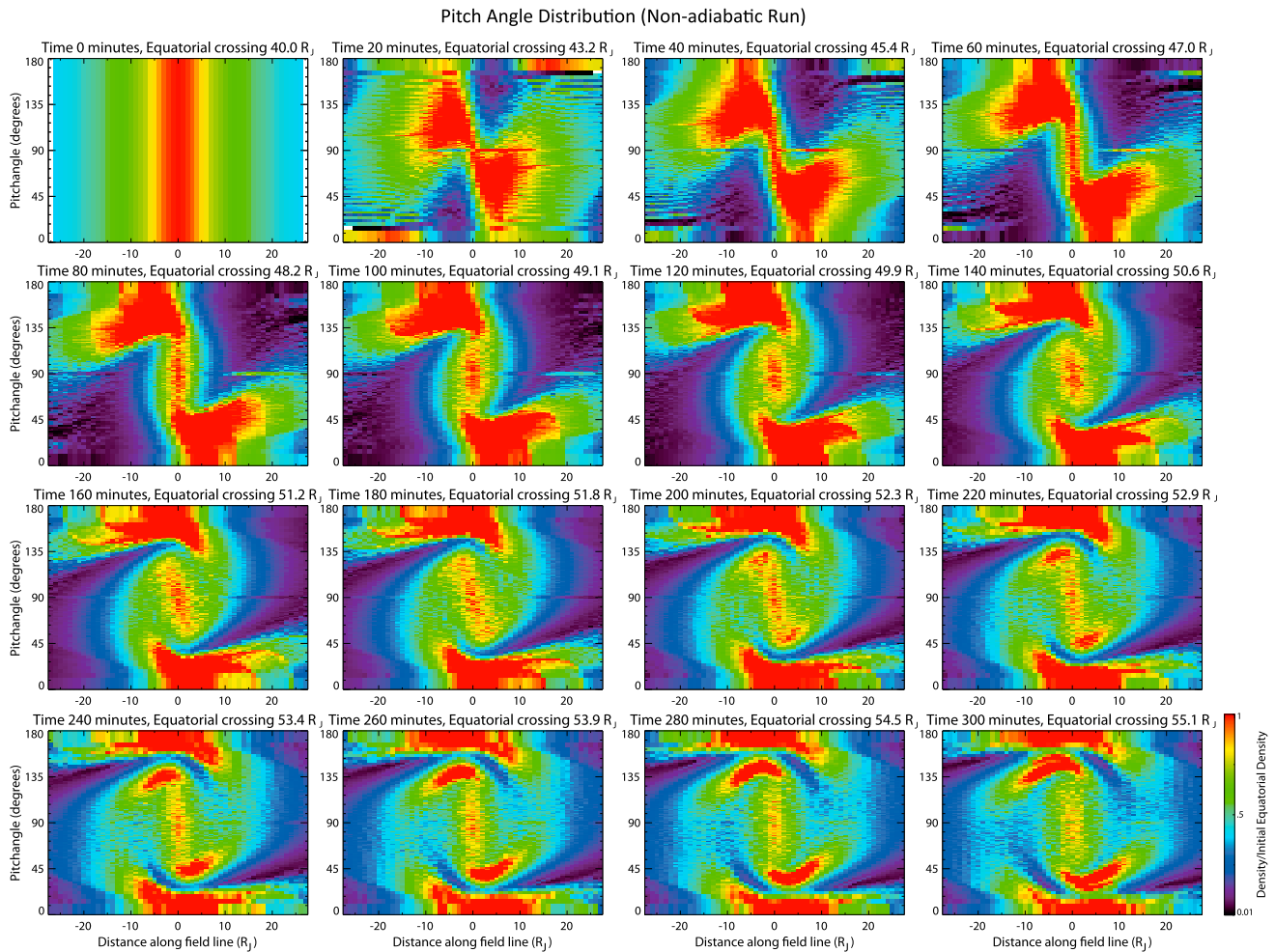
Figure 12. As in Figure 9, time evolution of the pitch angle distribution, as a function of distance along the field line but for the rapid stretching case (initial 4 keV kappa distribution). Overall, the pitch angle distribution becomes more field aligned at and near the equator as the flux tube expands outward.

and the flux tube length increases as it expands), the density decreases everywhere along the field line but its value decreases far more slowly near the equator than away from the equator. In fact, the *number* of particles at the equator within a fixed distance along the field increases as the flux tube moves out, but the density there decreases because the flux tube volume increases.

Figure 9 shows how the initially isotropic pitch angle distribution evolves, becoming more field-aligned as the flux tube moves out. Figure 10 illustrates how the energy distribution evolves in time under adiabatic stretching. There is a net decrease in energy everywhere along the flux tube as expected from conservation of μ and J. As the flux tube expands, the highest energies continue to be observed near the equator, where the centrifugal potential is largest, and the energy continues to fall off with distance along the field line as it does in the initial distribution.

5.2. Pitch Angle and Energy Evolution Under Rapid (Nonadiabatic) Stretching

Compared to the adiabatic stretching case, for which the particle distributions evolved smoothly, the results from the fast stretching case show far more complicated changes, with more variability on time scales close to the typical particle bounce periods. For example, the density distribution along the field line, plotted in Figure 11, always falls off with distance along the field line, but the degree to which the particles are centrifugally confined, or the effective scale height, does not change monotonically. At some times (100 and 200 min, corresponding to equatorial radial crossing distances of 49.1 and 52.3 R_J, respectively), the particles are highly concentrated at the equator and the density falls off sharply with distance along the field line,
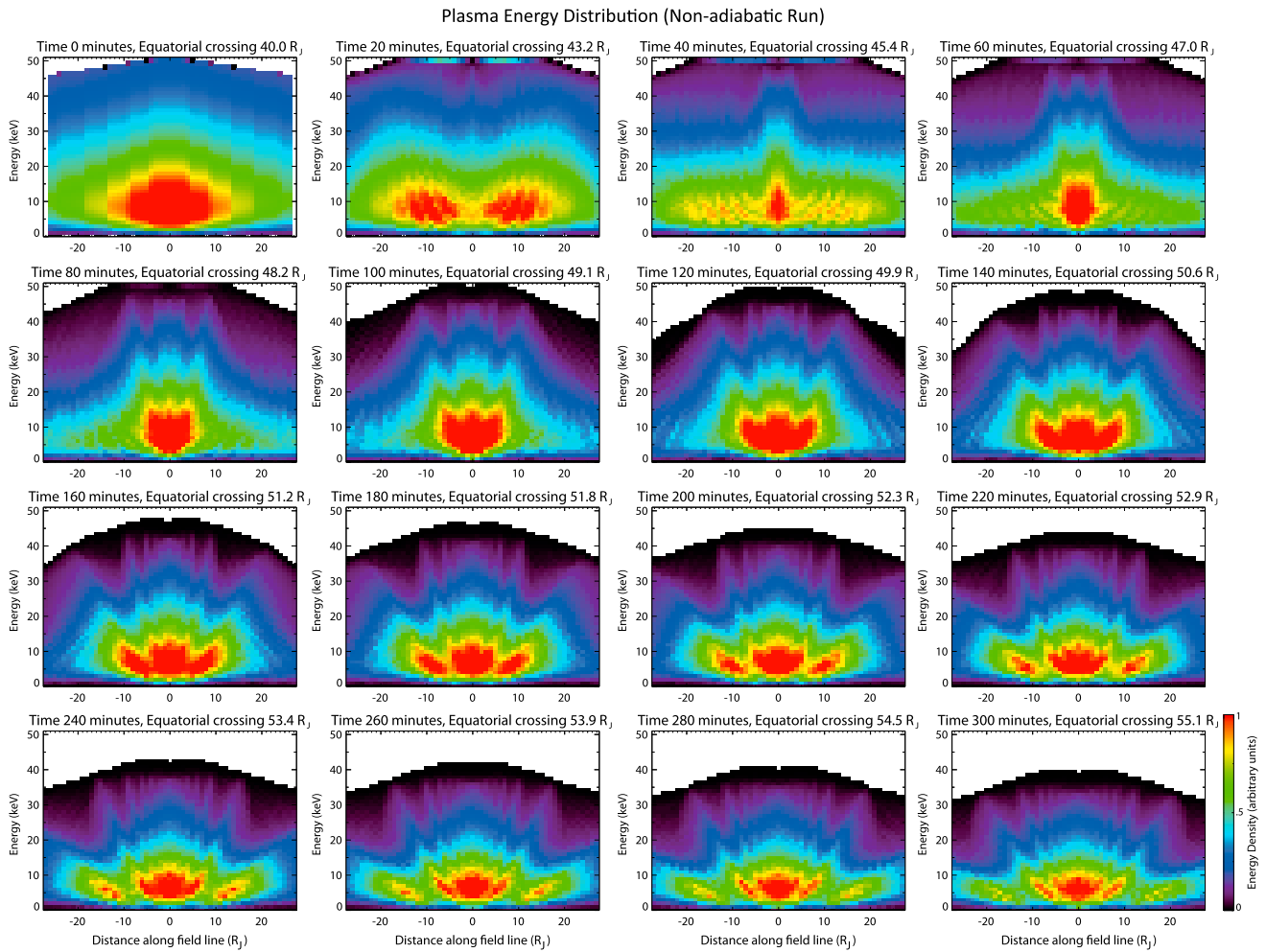
Figure 13. As in Figure 10, time evolution of the plasma energy distribution as a function of distance along the field line but for the nonadiabatic stretching case (initial 4 keV kappa distribution).

whereas at other times (50 and 300 min, or radial crossing distances of 46.2 and 55.1 R_J, respectively), the particles are more evenly spread along the field line.

This quasi-periodic (~1–2 h) rearrangement of the density along the flux tube seems to arise from the nonadiabatic nature of the flux tube expansion. The time scale appears to be related to the bounce periods of the simulated particles, which is typically a few hours (see Table 1). For example, the bounce period (on the initial flux tube) is ~2.5 h for a particle with an initial 60° equatorial pitch angle and 10 keV equatorial energy, which is close to the average initial equatorial energy of the simulated particles. The nonadiabatic nature of the flux tube expansion introduces this quasi-periodicity by accelerating some particles more than others, depending on their initial position. As mentioned in section 3.2, the increase in centrifugal potential energy as a particle moves out from a distance ρ to $\rho + \Delta\rho$ is proportional to $2\rho\Delta\rho$, meaning that as a flux tube expands nonadiabatically, particles that begin near the equator, at large ρ, gain more energy due to the centrifugal potential than particles that begin high along the field line, at small ρ. The initially near-equatorial particles therefore have more parallel energy than the off-equatorial particles and can move farther up along the field line than the initially off-equatorial particles can move down the field line toward the equator. This causes the equatorial density to decrease and the off-equatorial density to increase. Eventually, as particles continue their bounce motion, the density becomes more concentrated near the equator again.

The pitch angle and energy density distributions, seen in Figures 12 and 13, respectively, evolve with a periodicity similar to that seen in the time variation of number density along the field line. These figures show that initially (20 min, equatorial crossing distance 43.2 R_J) as the flux tube moves out, the pitch angle
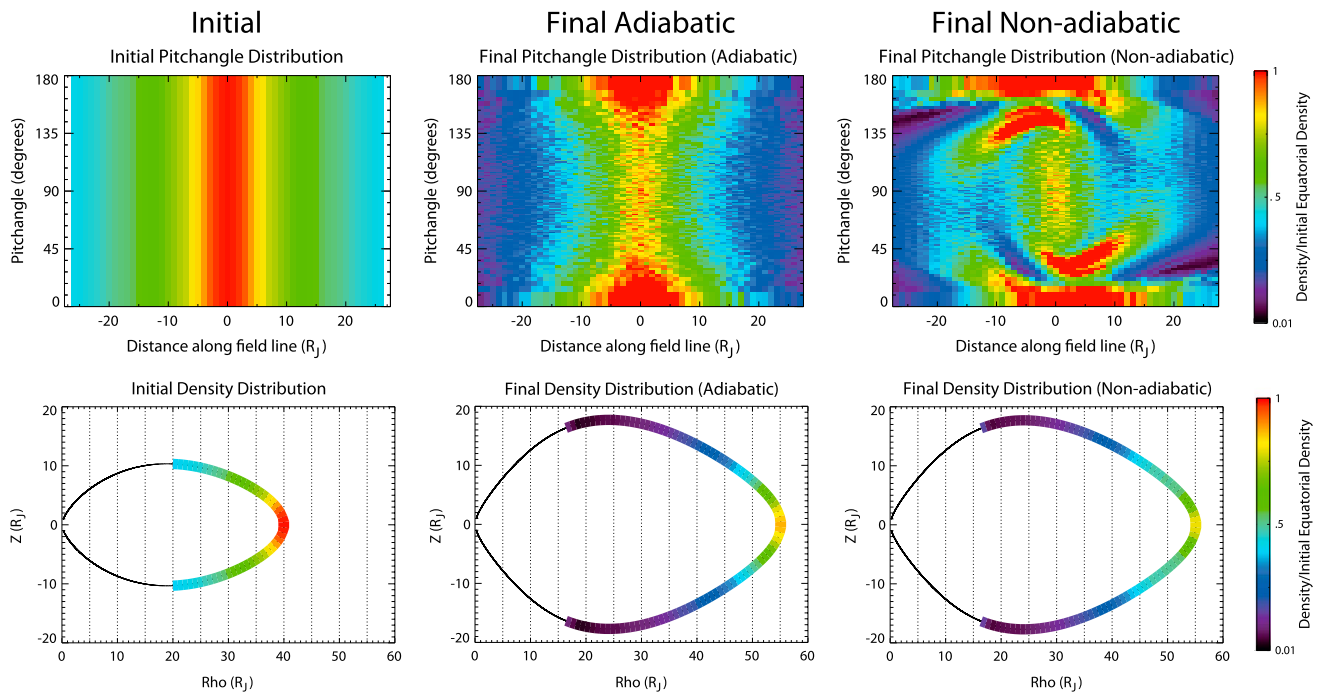
Figure 14. (top) Comparison of the final distributions of pitch angle versus distance along the field (following format of Figure 7) and (bottom) particle density along the field line (following format of Figure 6) for the adiabatic and fast stretching simulation runs (initial 4 keV kappa distribution).

distribution within 10 R_J of the equator becomes significantly more field-aligned. During the same interval, the energy density decreases close to the equator and increases near 10 R_J along the field. By comparison, the pitch angle and energy density distribution far (~15 R_J or more) off the equator show relatively little change, as expected since the particles that begin near the equator experience a larger increase in centrifugal potential energy, and corresponding pitch angle and energy changes, than the particles with initial positions far off the equator.

The clockwise, swirling evolution of the pitch angle distribution in Figure 12 that follows the onset of outward motion is consistent with the changes expected as particles bounce along the field. As a particle bounces along a field line from its mirror point to the equator, its pitch angle becomes increasingly field-aligned (or antifield-aligned) until the particle reaches the equator. As the particle continues to move along the field away from the equator, the pitch angle returns to 90° and the particle mirrors. This bounce motion results in a clockwise, elliptical motion through pitch angle/distance space similar to that seen in Figure 12. That the peaks of the pitch angle distribution follow this swirling motion is consistent with the idea that the initial outward motion redistributes the plasma along the field by energizing the outward moving near-equatorial particles, creating an off-equatorial density peak of particles. A pitch angle pattern very similar to that seen at 40 min reappears, noticeably at time ~200–220 min, as the plasma is redistributed along the field line, although at the later time the double-hooked pattern is confined to pitch angles near 90°. Overall, much as in the adiabatic case, the pitch angle distribution becomes more field-aligned as the flux tube moves radially outward, but here the anisotropy develops very early during the outward expansion and is more extreme than in the adiabatic stretching case.

The periodic density redistribution along the field line produces localized peaks in the energy distribution that shift to lower energies as the distribution moves against the centrifugal potential along the field line. For example, a peak in energy density near the equator at time 40 min (the green color near 25–30 keV in Figure 13) expands away from the equator in subsequent time steps. By time 180 min, the peak has shifted from ~5 to 15 R_J off the equator, and its energy has dropped to ~20 keV. As the flux tube moves out, the general structure of the energy distribution resembles a lotus flower, with localized density peaks off the equator corresponding to individual "petals" peeling away from the center.
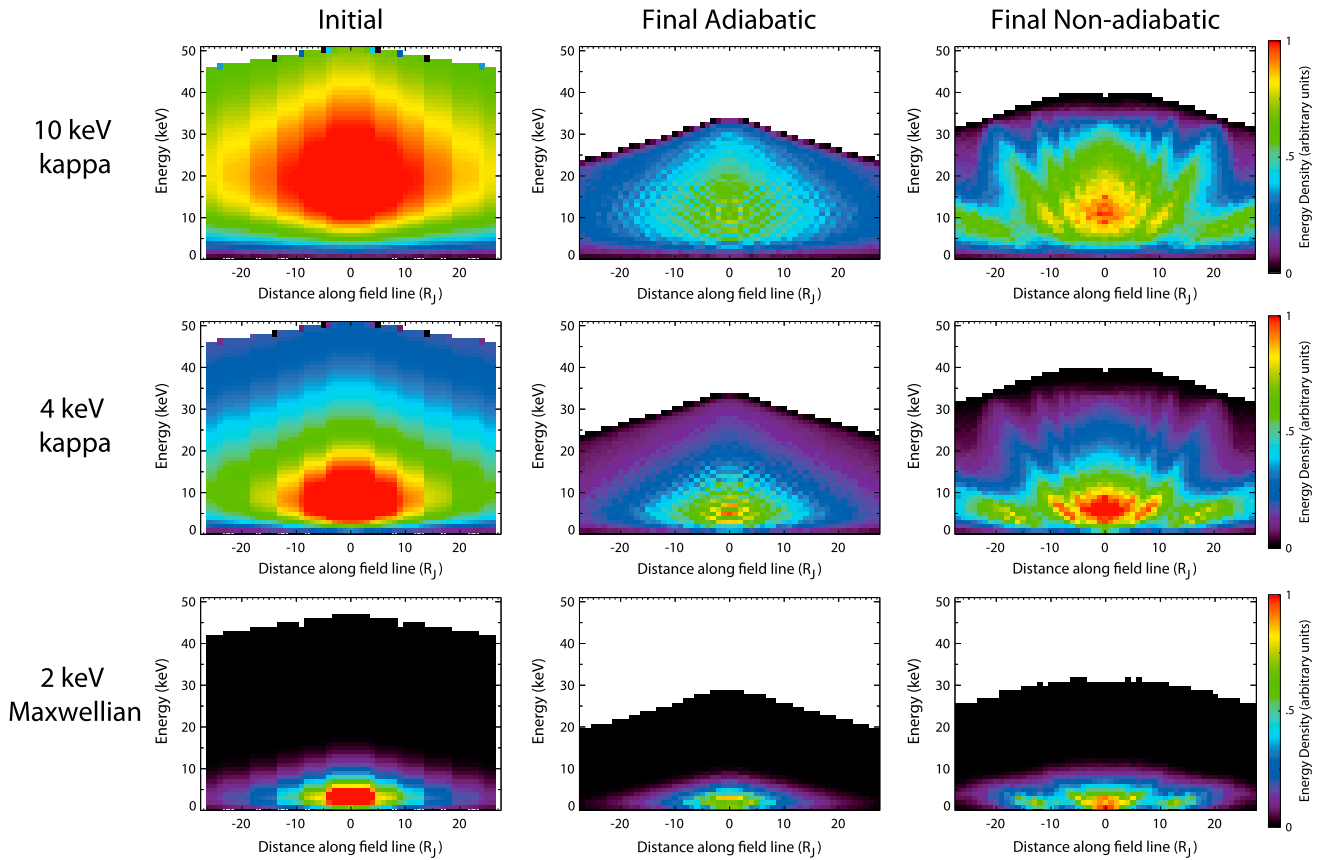
Figure 15. The initial and final energy density distributions as a function of energy versus distance along the field line for the adiabatic and nonadiabatic runs, assuming different initial energy distributions. (From top to bottom) A 10 keV kappa distribution, 4 keV kappa distribution (both with $\kappa = 3$), and 2 keV Maxwellian distribution. (From left to right) The plots of the initial distribution, the final distribution for rapid expansion, and the final distribution for slow expansion.

A comparison of the final pitch angle and density distributions for the adiabatic and nonadiabatic cases is shown in Figure 14, while Figure 15 (middle row) compares the final energy density distributions for the two cases with an initial 4 keV kappa distribution. Compared to the adiabatic case, the fast stretching case has more particles at large energies at all points along the field line, and the particles are less confined to the equator. In both cases, the pitch angle distribution has become field-aligned at the equator, though the anisotropy is greater in the nonadiabatic case.

6. Discussion

6.1. Plasma β Along the Field Line

We next consider whether the relative energy increase is sufficient to produce instability and account for the thickening of the plasma sheet observed in the transition from noon to dusk. To answer this question we examine quantitatively the evolution of the total thermal energy and the pressure anisotropy for the adiabatic and nonadiabatic cases.

Figure 16 shows the evolution of the plasma β, the ratio of the thermal to magnetic pressure, as a function of distance along the field line for the adiabatic and nonadiabatic cases. The initial values, plotted as black dashed lines, vary along the field line with a maximum at the equator where the density and average thermal energy are highest and the field magnitude is lowest. We normalized the particle density such that the initial equatorial $\beta = 6$, which is consistent with early observations from Jupiter's plasma sheet [*Walker et al.*, 1978; *McNutt*, 1983; *Kane et al.*, 1995], though slightly on the low end of estimates from the Galileo EPD [*Kane et al.*, 1999]. Figure 16 (top) shows plots of the plasma β for the first 30 min of the nonadiabatic expansion and the first 3000 min of the adiabatic case, times chosen to correspond to the same radial expansion of the flux tube. In the nonadiabatic case, both $\beta_{//}$ (black) and $\beta_{\perp}$ (green) initially decrease near the equator and a large
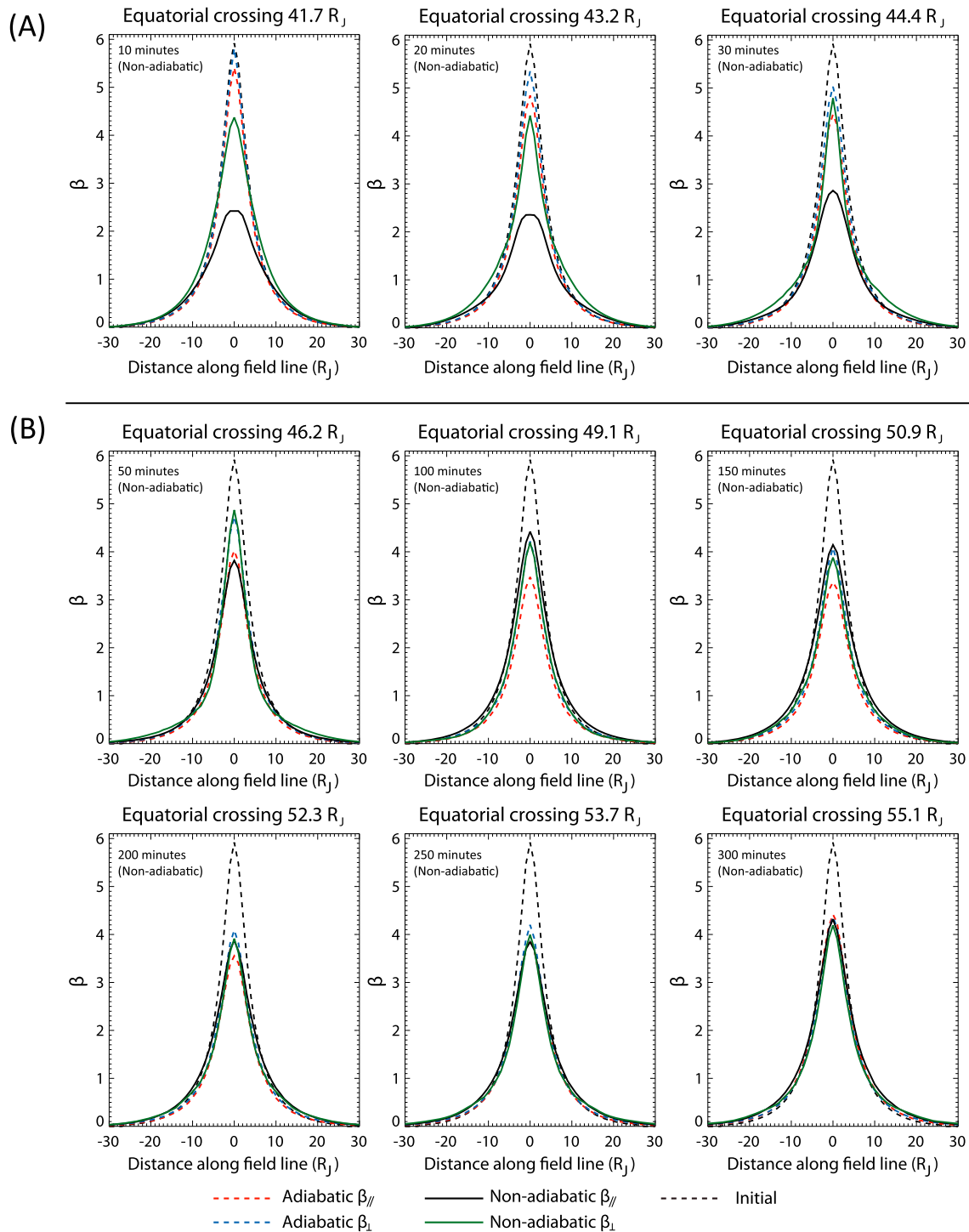
Figure 16. $\beta_{//}$ and $\beta_{\perp}$ as a function of distance along the field line for both the adiabatic case (red and blue dashed lines, respectively) and nonadiabatic case (black and green lines, respectively), all for an initial 4 keV kappa distribution. The black dashed line shows the initial values at $\rho_e = 40\ R_J$. (a) Changes to $\beta_{//}$ and $\beta_{\perp}$ as the flux tube expands outward over ~4.4 R_J, in 10 min (1000 min) increments for the nonadiabatic (adiabatic) case. (b) Changes to $\beta_{//}$ and $\beta_{\perp}$ for the full 15 R_J expansion, separated by 50 min (5000 min) increments for the nonadiabatic (adiabatic) case.

pressure anisotropy ($\beta_{\perp} > \beta_{//}$) develops near the equator; off the equator, $\beta_{\perp}$ increases for the nonadiabatic case as the off-equatorial particle density increases, while the equatorial $\beta_{//}$ decreases. The increase in $\beta_{\perp}$ would cause the field to become more dipolar, while the decrease in $\beta_{//}$ would diminish the radially stretched nature of the field structure, already in early stages of the flux tube expansion, which is consistent with a
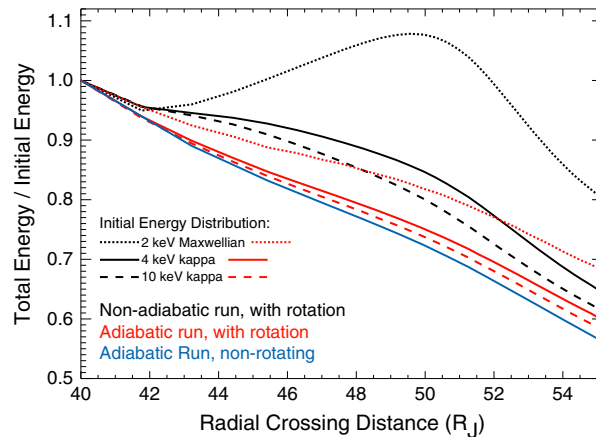
Figure 17. Evolution of the total flux tube energy content, normalized to the initial value and plotted versus flux tube equatorial crossing distance. Shown is the flux tube energy content for an initial 2 keV Maxwellian (dotted), 4 keV kappa (solid), and 10 keV kappa distribution (dashed), both for the adiabatic (red) and nonadiabatic (black) stretching rates, in a rotating system. The blue line indicates total flux tube energy content for an outward moving flux tube in a nonrotating system.

thicker plasma sheet. In the adiabatic case, the equatorial pressure anisotropy that develops is relatively small by comparison, and there is also little or no pressure anisotropy off the equator. At later times and larger distances (Figure 16, bottom), the equatorial $\beta_{//}$ and $\beta_\perp$ decrease (but nonmonotonically) for both the adiabatic and nonadiabatic cases. The off-equatorial $\beta_{//}$ and $\beta_\perp$ increase for both cases, with very little pressure anisotropy in the adiabatic case. Near the equator (beyond a radial equatorial crossing distance of ~53 R_J), there is little or no pressure anisotropy for either the adiabatic or nonadiabatic case late in the flux tube expansion. We note that for both the adiabatic and nonadiabatic cases, there is relatively little pressure anisotropy in the final three time steps shown in Figure 16, though the pitch angle distributions show a largely field-aligned distribution (see Figures 9 and 12). This is because the centrifugal force most strongly influences the lower energy (quasi-Maxwellian, $< \sim10\,\text{keV}$) part of the energy distribution, which dominates the number density, leading to an anisotropic pitch angle distribution, while the higher-energy ($> \sim10\,\text{keV}$) particles dominate the energy density.

That a larger pressure anisotropy develops in the nonadiabatic case than in the adiabatic case is a key point in considering the stability of the plasma sheet, as was discussed in section 2.2. The observed changes in energy density, $\beta_{//}$, and $\beta_\perp$ are all consistent with the nonadiabatic effects producing conditions that would cause field dipolarization, which in turn is consistent with a thickening of the plasma sheet. However, the calculation has not been carried out self-consistently, so that the plasma pressure has not been allowed to modify the modeled field configuration.

6.2. Effect of Initial Energy Distribution

Our choice for the initial plasma energy distribution affects the outcome of the field expansion process. For the results presented in section 5, we formed the initial equatorial distributions by weighting the simulated particles according to an isotropic kappa distribution with a mean energy of 4 keV. Because of the uncertainty of the form of the distribution, we have also investigated the response of two other distributions consistent with the published results: a 2 keV Maxwellian and a 10 keV kappa distribution ($\kappa = 3$).

The final energy density distributions for the adiabatic and nonadiabatic cases, for the three different initial temperature distributions, are given in Figure 15. For each of the three initial temperature choices, the final nonadiabatic energy distribution shows an enhanced energy density at high energies and at off-equatorial positions compared to the final adiabatic distribution.

Figure 17 shows how the total flux tube energy content (normalized to the initial value) varies with equatorial crossing distance for various situations considered in this study and for adiabatic expansion of an isotropic distribution in a nonrotating system. The initial distribution for the nonrotating case is derivable from equation (17) or (20) by setting $\Omega = 0$. For all cases the outward flux tube expansion eventually results in lower total energy, though the fractional energy decrease is smaller for the nonadiabatic case than for adiabatic expansion. The difference between the adiabatic and nonadiabatic energy content is largest for the 2 keV Maxwellian (dotted lines) and smallest for the 10 keV kappa (dashed lines), as expected because a higher mean energy gives greater weight to the particles that behave most adiabatically. In fact, for the nonadiabatic run with a 2 keV Maxwellian initial distribution, the total energy content even shows a net increase in energy at equatorial crossing distances between ~45 and ~52 R_J, with a peak of ~1.1 times the initial energy content.

Not surprisingly, without the contribution from the centrifugal potential, the flux tube energy content in the nonrotating system decreases more rapidly with outward distance than in any of the adiabatic or nonadiabatic runs in the rotating system. Finally, we also note that the energy content of the adiabatic runs in the rotating system approaches the values for adiabatic expansion in the nonrotating system as the initial mean energy increases. The reason is that a displacement from 40 R_J to ~55 R_J corresponds to a change of only ~23 keV of centrifugal potential energy. If the initial plasma mean energy is many tens of keV or larger, the effect of this small change of centrifugal potential will be small for both adiabatic and nonadiabatic flux tube expansions.

7. Summary and Conclusions

In this study we developed a quantitative model to determine the effects of nonadiabatic field line stretching and rapid rotation on pitch angle and energy distributions. The large spatial scales in Jupiter's magnetosphere and rapid planetary rotation period make the centrifugal force important to particle dynamics. *Kivelson and Southwood* [2005] suggested that centrifugal effects are responsible for the thickening of the plasma sheet that occurs as flux tubes expand from noon to dusk. A key point in the Kivelson and Southwood idea is that bounce periods are long compared to the ~5 h time scale for field line stretching between noon and dusk, and that consequently, bounce motion may violate the second adiabatic invariant. We tested the Kivelson and Southwood hypothesis using an LSK simulation that followed a collection of particles as they moved along a rotating, stretching flux tube, and examined the changes to the particle energy and pitch angle distributions. We used realistic spatial and time scales and a steady state initial plasma distribution with a realistic energy distribution, in order to quantitatively describe the effects of rapid expansion of a rotating flux tube. This simulation was meant as a proof of principle for the physical processes that occur in Jupiter's magnetosphere between noon and dusk, so we only followed particles beginning on one flux tube. Furthermore, the simulation was not carried out self-consistently. We did not use plasma distributions that were in perpendicular force balance with the model magnetic field, nor did we allow the particle distributions to be modified by pitch angle scattering.

We ran the simulation with two different field line stretching time scales: a realistic but nonadiabatic 5 h characteristic of the time for a flux tube to rotate from noon to dusk in the middle Jovian magnetosphere and a 500 h time scale, which was long enough to conserve the second adiabatic invariant. The adiabatic run provided a baseline to show which changes in the nonadiabatic run were due to the speed of the field line stretching and which were due simply to outward expansion. Our results show that the response of plasma to flux tube expansion in a rotating magnetosphere depends on a variety of factors including the initial energy, pitch angle, and spatial distributions of the plasma, whether the expansion proceeds adiabatically or nonadiabatically, and how the loss of perpendicular energy due to betatron acceleration and parallel energy due to Fermi acceleration compares to the addition of centrifugal potential energy. For a sufficiently low mean energy in the initial distribution (not inconsistent with some estimates of the plasma properties of the Jovian plasma sheet), the expansion of a rotating flux tube can even produce a net increase of the total energy of the plasma on the flux tube at some time during the expansion.

Analysis of the pitch angle, energy, and spatial distributions for the runs shows that the distributions changed as expected under adiabatic expansion: the pitch angle distribution became more field-aligned, particles became increasingly confined to the equator, and the energy decreased. However, under nonadiabatic expansion, the changes were much more complex and for an initial 2 keV Maxwellian mean energy distribution, the total energy of the plasma even showed a brief increase. Compared to the adiabatic run, the nonadiabatic case resulted in a larger pitch angle anisotropy that developed earlier in the outward expansion, accelerated more particles to high energies, and increased the density of particles at off-equatorial positions (less centrifugal confinement). A larger pressure anisotropy developed for the nonadiabatic case than for the adiabatic case, suggesting that the rapid stretching may lead to plasma instability which would affect the structure of the plasma sheet and the magnetic field threading it. A comparison of the calculated changes to the pitch angle and energy distributions and the energy density in the nonadiabatic case compared to those in the adiabatic case suggests that the nonadiabatic effects contribute to field dipolarization and plasma sheet thickening. The calculations were not performed self-consistently, but they allow one to conclude that the effects of centrifugal acceleration change the plasma distribution in ways that would

require the field to reconfigure and become more dipolar. Consequently, we conclude that the idea of *Kivelson and Southwood* [2005] that non-adiabatic effects in Jupiter's rapidly rotating magnetosphere are likely to contribute to field dipolarization and instability of the plasma sheet, and that centrifugal acceleration combined with radial expansion is a plausible explanation for the observed plasma sheet thickening between noon and dusk.

Appendix A: Particle Drift and Bounce Motion in the Rotating Frame

The first adiabatic invariant, μ, is the magnetic moment and is conserved in the rotating frame under the assumptions that the time scale for changes in the magnetic field is long compared with a gyroperiod and that the gyroradius is small compared to the scale length for changes in the magnetic field (such as the radius of curvature). The second adiabatic invariant is the sum of the parallel momentum over a complete bounce period:

$$J = \oint_S m v_\parallel ds,\tag{A1}$$

where s is the distance along the field and $v_{//}$ is the parallel velocity in the guiding center frame [*Northrop*, 1963]. J is conserved only if the magnetic field changes slowly compared to the bounce period. *Northrop and Birmingham* [1982] showed that J is conserved in the rotating frame for the general case of a rigidly rotating magnetic field, time stationary in the rotating frame, at an arbitrary angle to Ω in the absence of a parallel electric field.

The Lorenz force equation dictates particle motion. In the rotating frame, it is given by

$$m\frac{d\mathbf{v}}{dt} = q(\mathbf{E} + \mathbf{v} \times \mathbf{B}) - m(2\mathbf{\Omega} \times \mathbf{v} + \mathbf{\Omega} \times (\mathbf{\Omega} \times \mathbf{r})),\tag{A2}$$

where $\mathbf{v}$ is the particle velocity in the rotating frame and it is assumed that particles are rigidly corotating with the magnetic field with angular frequency Ω. The effects of rotation are included by two terms in equation (A2): the Coriolis force, $-2m(\Omega \times \mathbf{v})$, and the centrifugal force. The Coriolis force has no effect on particle energy in the guiding center frame because it is perpendicular to the particle motion and therefore does no work (but does introduce an azimuthal drift averaged over a gyroperiod).

The centrifugal force, which can be written as the gradient of a centrifugal potential $\nabla \frac{1}{2}\rho^2\Omega^2$, does affect the particle energy. In the absence of an electric field, $(|\mathbf{v}|^2 - \rho^2\Omega^2)$ is a constant of the particle motion (K), which can also be written as

$$K \equiv \frac{m}{2}\left(w_\parallel - \rho^2\mathbf{\Omega}^2\right) + \mu B\tag{A3}$$

[*Northrop and Birmingham*, 1982]. (Note that constancy of K requires that the conditions required to conserve μ and J are met and assumed the absence of an electric field, though a constant of the particle motion may still be defined for an arbitrary electric field that satisfies $\mathbf{E} \cdot \mathbf{B} = 0$ and $\nabla \times \mathbf{E} = 0$.) Equation (A3) shows how a particle bouncing on a magnetic field line in a field that is time stationary in the rotating frame will gain and lose kinetic energy as it moves through the centrifugal potential during a bounce period. Furthermore, it shows that the centrifugal force affects only the parallel component of particle energy. The perpendicular component of the centrifugal force produces a guiding center drift, but this drift does not affect the particle energy in the guiding center frame.

In planetary magnetic fields, the centrifugal force concentrates particles near the centrifugal equator by restricting inward motion: particles reach their maximum total energy at the point along the field line that is farthest from the planet but lose parallel energy as they move along the field line to smaller ρ. This loss of parallel energy causes particles to mirror farther from the planet (closer to the centrifugal equator) than they would in the absence of rotation, so that plasma density is highest at the centrifugal equator and falls off exponentially with distance along the field line [e.g., *Hill and Michel*, 1976; *Bagenal et al.*, 1980; *Bagenal and Sullivan*, 1981]. Figure A1 illustrates how the centrifugal force affects particle bounce motion and energy by altering the parallel energy during a bounce period and confining particles to the centrifugal equator.
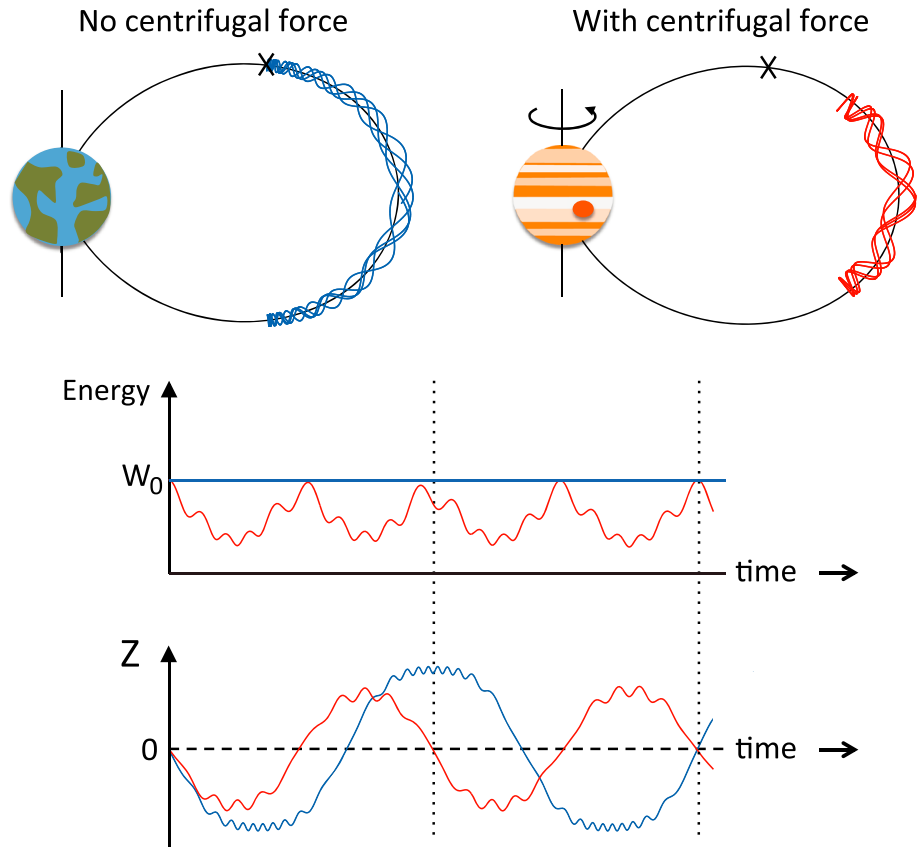
Figure A1. Illustration of how the centrifugal force affects particle bounce motion and energy. (top) The particle bounce trajectory in the meridian plane for two example particles with the same equatorial energy and pitch angle in the (left) absence and (right) presence of centrifugal force. The centrifugal force restricts particle motion up the field, so that the rotating particle (red) mirrors farther from the planet and remains confined near the centrifugal equator; the location of the mirror point for the nonrotating case is marked with an X. (middle) The energy of the example particles as a function of time. (bottom) The particle z position as a function of time; in these plots the example particles begin at the equator with the same pitch angle and energy. In the nonrotating case (blue), the particle energy remains constant, whereas the particle on a rotating flux tube loses energy to the centrifugal force as it travels along the field to smaller ρ. The small oscillations in Figure A1 (middle and bottom) occur during a gyroperiod.

Appendix B: Adiabatic Flux Tube Expansion for a Nonrotating, Static Magnetic Field

As mentioned in section 3.1, adiabatic flux tube expansion for a time stationary magnetic field occurs due to an $\mathbf{E} \times \mathbf{B}$ drift, where the electric field is derivable from a scalar potential ϕ. For the case of a nonrotating flux tube, the constant of motion analogous to that from equation (3) is given by

$$C_i \equiv \frac{m}{2}(w_{\parallel}) + \mu B + q\phi, \tag{B1}$$

where w is the velocity in the inertial frame and the subscript i denotes the inertial frame. Conservation of μ implies that perpendicular energy decreases under adiabatic flux tube expansion to a larger radial distance, where the magnetic field is weaker. This process is known as betatron acceleration. Conservation of J requires that the parallel energy change through Fermi acceleration if the distance between mirror points changes. The change in parallel energy therefore depends in part on the magnetic field geometry. In general, as a flux tube expands to larger ρ, the length of the field line and the distance between mirror points both increase, so the parallel energy decreases. For expansion of a dipole field the change in parallel energy, $W_{//}$, follows

$$\frac{W_{\parallel}}{W_{\parallel,0}} = \left(\frac{L_0}{L}\right)^{\chi}, \tag{B2}$$

where the 0 subscript indicates initial values and χ varies between 2.0 and 2.5 for different initial equatorial pitch angles [*Southwood and Kivelson*, 1975]. Therefore, we expect both the perpendicular and parallel energies to decrease during adiabatic expansion of a nonrotating flux tube to a larger radial distance. This net kinetic energy loss requires drift to a larger ϕ to conserve the total energy in equation (B1).

References

Ashour-Abdalla, M., J. P. Berchem, J. Büchner, and L. M. Zelenyi (1993), Shaping of the magnetotail from the mantle: Global and local structuring, *J. Geophys. Res.*, 98, 5651–5686.

Bagenal, F., and J. D. Sullivan (1981), Direct plasma measurements in the Io torus and inner magnetosphere of Jupiter, *J. Geophys. Res.*, 86, 8447–8466.

Bagenal, F., J. D. Sullivan, and G. L. Siscoe (1980), Spatial distribution of plasma in the Io torus, *Geophys. Res. Lett.*, 7, 41–44.

Behannon, K. W., L. F. Burlaga, and N. F. Ness (1981), The Jovian magnetotail and its current sheet, *J. Geophys. Res.*, 86, 8385–8401.

Belcher, J. W. (1983), The low energy plasma in the Jovian magnetosphere, in *Physics of the Jovian Magnetosphere*, edited by A. J. Dessler, pp. 68–105, Cambridge Univ. Press, Cambridge, U. K., doi:10.1017/CBO9780511564574.005.

Birmingham, T. J., and T. G. Northrop (1979), Theory of flux anisotropies in a guiding center plasma, *J. Geophys. Res.*, 84, 41–45.

Büchner, J., and L. M. Zelenyi (1989), Regular and chaotic charged particle motion in magnetotaillike field reversals: 1. Basic theory of trapped motion, *J. Geophys. Res.*, 94, 11,821–11,842, doi:10.1029/JA094iA09p11821.

Cowley, S. W. H., E. J. Bunce, T. S. Stallard, and S. Miller (2003), Jupiter's polar ionospheric flows: Theoretical interpretation, *Geophys. Res. Lett.*, 30(5), 1220, doi:10.1029/2002GL016030.

Frank, L. A. and W. R. Paterson (2002), Galileo observations of electron beams and thermal ions in Jupiter's magnetosphere and their relationship to the auroras, *J. Geophys. Res.*, 107(A12), 1478, doi:10.1029/2001JA009150.

Frank, L. A., and W. R. Paterson (2004), Plasmas observed near local noon in Jupiter's magnetosphere with the Galileo spacecraft, *J. Geophys. Res.*, 109, A11217, doi:10.1029/2002JA009795.

Frank, L. A., K. L. Ackerson, J. A. Lee, M. R. English, and G. L. Pickett (1992), The plasma instrumentation for the Galileo mission, *Space Sci. Rev.*, 60, 283–307.

Gledhill, J. A. (1967), The structure of Jupiter's magnetosphere and the effect of Io on its decametric radio emission, *NASA Tech. Memo. X-55980*, *NASA/GSFC X Doc. 615-67-296*.

Goertz, C. K., A. W. Schardt, J. A. Van Allen, and J. L. Parish (1979), Plasma in the Jovian current sheet, *J. Geophys. Res.*, 6, 495–498.

Hill, T. W., and F. C. Michel (1976), Heavy ions from the Galilean satellites and the centrifugal distortion of the Jovian magnetosphere, *J. Geophys. Res.*, 81, 4561–4565.

Huang, T. S., and T. J. Birmingham (1992), The polarization electric field and its effects in an anisotropic rotating magnetospheric plasma, *J. Geophys. Res.*, 97, 1511–1519.

Joy, S. P., M. G. Kivelson, R. J. Walker, K. K. Khurana, C. T. Russell, and T. Ogino (2002), Probabilistic models of the Jovian magnetopause and bow shock locations, *J. Geophys. Res.*, 107(A10), 1309, doi:10.1029/2001JA009146.

Kane, M., B. H. Mauk, E. P. Keath, and S. M. Krimigis (1995), Hot ions in Jupiter's magnetodisc: A model for Voyager 2 low-energy charged particle measurements, *J. Geophys. Res.*, 100, 19,473–19,486.

Kane, M., D. J. Williams, B. H. Mauk, R. W. McEntire, and E. C. Roelof (1999), Galileo energetic particles detector measurements of hot ions in the neutral sheet region of Jupiter's magnetodisk, *Geophys. Res. Lett.*, 26, 5–8.

Khurana, K. K. (1992), A generalized hinged-magnetodisc model of Jupiter's nightside current sheet, *J. Geophys. Res.*, 97, 6269–6276.

Khurana, K. K. (1997), Euler potential models of Jupiter's magnetospheric field, *J. Geophys. Res.*, 102, 11,295–11,306.

Khurana, K. K., and M. G. Kivelson (1989), On Jovian plasma sheet structure, *J. Geophys. Res.*, 94, 11,791–11,803.

Khurana, K. K., and H. K. Schwarzl (2005), Global structure of Jupiter's magnetospheric current sheet, *J. Geophys. Res.*, 110, A07227, doi:10.1029/2004JA010757.

Khurana, K. K., M. G. Kivelson, V. M. Vasyliūnas, N. Krupp, J. Woch, A. Lagg, B. H. Mauk, and W. S. Kurth (2004), The configuration of Jupiter's magnetosphere, in *Jupiter: The Planet, Satellites, and Magnetosphere*, edited by F. Bagenal et al., chap. 24, Cambridge Univ. Press, New York.

Kivelson, M. G., and K. K. Khurana (2002), Properties of the magnetic field in the Jovian magnetotail, *J. Geophys. Res.*, 107(A8), 1196, doi:10.1029/2001JA000249.

Kivelson, M. G., and D. J. Southwood (2005), Dynamical consequences of two modes of centrifugal instability in Jupiter's outer magnetosphere, *J. Geophys. Res.*, 110, A12209, doi:10.1029/2005JA011176.

Krimigis, S. M., J. F. Carbary, E. P. Keath, C. O. Bostrom, W. I. Axford, G. Gloeckler, L. J. Lanzerotti, and T. P. Armstrong (1981), Characteristics of hot plasma in the Jovian magnetosphere: Results from the Voyager spacecraft, *J. Geophys. Res.*, 86, 8227–8257.

Krupp, N., A. Lagg, S. Livi, B. Wilken, J. Woch, E. Roelof, and D. Williams (2001), Global flows of energetic ions in Jupiter's equatorial plane: First-order approximation, *J. Geophys. Res.*, 106, 26,017–26,032.

Lanzerotti, L. J., et al. (1993), *Planet. Space Sci.*, 41, 893–917.

Lanzerotti, L. J., et al. (1993), Measurements of hot plasmas in the magnetosphere of Jupiter, *Planet. Space Sci.*, 41, 893–917.

McNutt, R. L., Jr. (1983), Force balance in the magnetospheres of Jupiter and Saturn, *Adv. Space Res.*, 3, 55–58.

McNutt, R. L., Jr., J. W. Belcher, and H. S. Bridge (1981), Position ion observations in the middle magnetosphere of Jupiter, *J. Geophys. Res.*, 86, 8319–8342, doi:10.1029/JA086iA10p08319.

Northrop, T. G. (1963), *The Adiabatic Motion of Charged Particles*, InterScience, New York.

Northrop, T. G., and T. J. Birmingham (1982), Adiabatic charged particle motion in rapidly rotating magnetospheres, *J. Geophys. Res.*, 87, 661–669.

Northrop, T. G., and E. Teller (1960), Stability of the adiabatic motion of charged particles in the Earth's field, *Phys. Rev.*, 117(1), 215–225.

Pierrard, V., and J. Lemaire (1996), Lorentzian ion exosphere model, *J. Geophys. Res.*, 101, 7923–7934.

Southwood, D. J., and M. G. Kivelson (1975), An approximate analytic description of plasma bulk parameters and pitch angle anisotropy under adiabatic flow in a dipolar magnetospheric field, *J. Geophys. Res.*, 80, 2069–2073.

Treumann, R. A., and W. Baumjohann (2001), *Advanced Space Plasma Physics*, Imperial College Press, London, U. K.

Vasyliūnas, V. M. (1968), A survey of low-energy electrons in the evening sector of the magnetosphere with OGO 1 and OGO 3, *J. Geophys. Res.*, 73, 2839–2884.

Vasyliūnas, V. M. (1983), Plasma distribution and flow, in *Physics of the Jovian Magnetosphere*, edited by A. J. Dessler, pp. 395–453, Cambridge Univ. Press, New York.

Waldrop, L. S., T. A. Fritz, M. G. Kivelson, K. Khurana, N. Krupp, and A. Lagg (2005), Jovian plasma sheet morphology: Particle and field observations by the Galileo spacecraft, *Planet. Space Sci.*, 53, 681–692.

Walker, R. J., M. G. Kivelson, and A. W. Schardt (1978), High β plasma in the dynamic Jovian current sheet, *Geophys. Res. Lett.*, 5, 799–802.

Williams, D. J., R. W. McEntire, S. Jaskulek, and B. Wilken (1992), The Galileo energetic particles detector, *Space Sci. Rev.*, 60, 385–412.